Predicting Net Surface Radiation for Alpine Surface Types Using Linear Models and Artificial Neural Networks

The Effect of Non-Corresponding Flux Footprints for the Energy Balance Closure at a Heterogeneous Surface

Eirik Næsset Ramtvedt

Master Thesis in Geoscience
Discipline: Meteorology and Oceanography
Department of Geoscience
Faculty of Mathematics and Natural Science
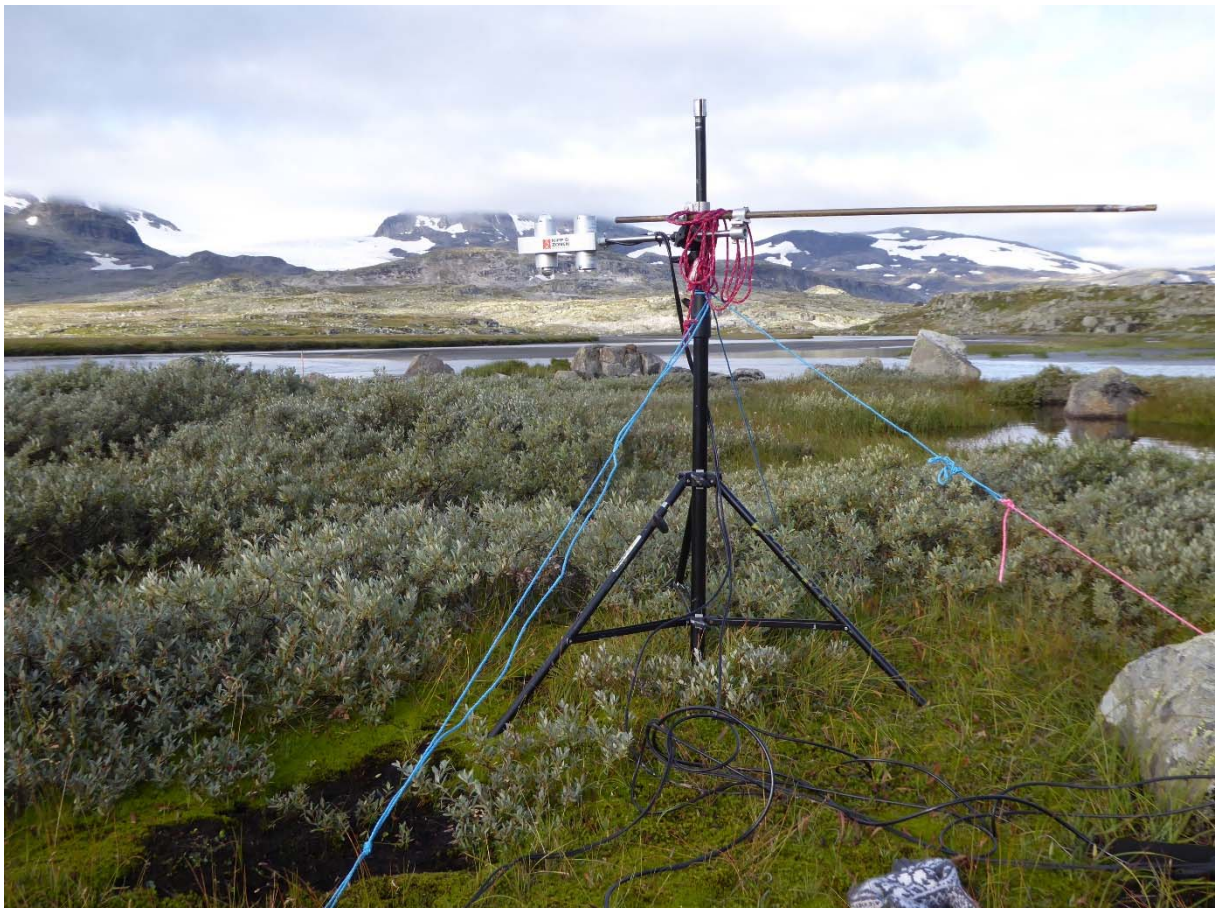30 credits

UNIVERSITY OF OSLO

October 2018

Predicting Net Surface Radiation for Alpine Surface Types Using Linear Models and Artificial Neural Networks

The Effect of Non-Corresponding Flux Footprints for the Energy Balance Closure at a Heterogeneous Surface

Eirik Næsset Ramtvedt

Predicting Net Surface Radiation for Alpine Surface Types Using Linear Models and Artificial Neural Networks

Abstract

Flux towers provide important climatic information about surface exchange processes in the land-atmosphere system. At the Finse flux tower in alpine Norway, the inhomogeneous surface and hilly terrain influence the quality of the eddy covariance (EC) measurements. Due to the large variation in surface cover, including bare ground, different vegetation types, and open water, it is challenging to provide a representative estimation of net surface radiation around the flux tower.

This study investigates the effect of non-corresponding footprints between the net surface radiation and the turbulent fluxes measured with the EC technique. This was done by measuring net surface radiation for different surface types, where the surface types were provided from a detailed vegetation map over the Finse study site. By fitting linear regression models (LMs) and training artificial neural networks, continuous time series of net surface radiation for different surface types for the period 18.08.18 – 25.08.18 where predicted. The time series from the LM were used to derive an overall value of net surface radiation, $\tilde{R}_{net}$, which accounted for the heterogeneity of the surface cover. Doing so, a better comparable value of net surface radiation was obtained for the evaluation of the surface energy balance closure.

Based on the linear model predictions, the study found a difference, with statistical significance of 99%, in net surface radiation between almost all the alpine surface types investigated. This implies that considerable differences of albedo and properties controlling the emissions of longwave radiation, occur in the surface cover which contributes as source area to the measurements of the turbulent fluxes. The energy balance ratio was found to be 58% when evaluated with the LM predicted $\tilde{R}_{net}$. Thus, the energy balance closure increased by 4.40 percent points when allowing for the effect of surface heterogeneity on the net surface radiation. However, when the energy balance closure was evaluated with the ordinary least squares regression technique, the closure was found to be only 37%. No improvement of the energy balance closure was found when the heterogeneity of surface cover was allowed for by this evaluation method. The work presented here is a proof-of-concept study, showing how heterogeneity at flux sites can be accounted for using the methodology presented.

Acknowledgements

First and foremost, I want to thank my supervisors Norbert Pirk and Frode Stordal for introducing me to this interesting field within climate research, and to have the confidence to let me take the project where I wanted. Norbert, your knowledge about the eddy covariance system and Finse flux tower has been crucial in the work with accomplishing this project. Thank you!

Secondly, thanks to Anders Bryn and Peter Horvath for helping me with the classification of the nature types at Finse, and for contributing with data and knowledge about the vegetation.

I am also grateful to Anne Claire Fouillox and Ana Costa Conrado for introducing me to artificial intelligence. Your assistance with the artificial neural network was very valuable to me.

Additionally, I would like to express gratitude to John Hult for technical help with the mobile radiation tower. Your technical expertise was very useful when you adapted the necessary instruments specially for this study.

I would also like to thank Finse Research Station and Erika Leslie for the accommodation during the fieldwork at Finse.

Finally, huge thanks to my nearest friends and family for encouraging and supporting me through the time of this project. It meant a lot!

Content

1   Introduction

Net surface radiation (R_{net}) constitutes the fundamental parameter controlling the climate in the lower atmosphere (Iziomon et al., 2000). The parameter plays an important role in the land-atmosphere interaction by determining the amount of energy available for sensible heat (H), latent heat (LE), soil heat (G), net advected energy (A_d), and storage of energy (S_t) – both physical and biochemical. For a heterogenous land surface, the energy balance will vary among the different surface patches. This is dependent on the unique interactions between surface albedo, vegetation physiology, the biogeochemical cycling and the state of the atmospheric boundary layer (Majozi et al., 2017).

Because of climate change, changes in terrestrial ecosystems and vegetation are leading to a changed land cover. Especially at high latitudes in the northern hemisphere, where the influence of global warming is more predominant than in other regions, we experience rapid land surface changes. Studies that have investigated the vegetation in Arctic biomes, clearly observed expansions of shrubs and trees since the 1950s and 1960s (Myers-Smith et al., 2015; Frost and Epstein, 2014). To further improve the understanding of local and regional climate change at high northern latitudes, and how the feedback mechanisms in the land-atmosphere system are developing, knowledge about the surface energy exchange is needed. A precise estimation of the net surface radiation for different land covers is therefore essential as an important input for climate processes, modeling and validation.

Despite the importance of R_{net}, the parameter is measured only at a few metrological stations. This is partly due to problems of providing a standard surface, but also because the net radiometers used to measure R_{net}, at least in the past, were difficult and time consuming to maintain and calibrate (Monteith and Unsworth, 2013). Therefore, different regression models for calculating net surface radiation from other climatic parameters are widely used (Kjaersgaard et al. 2007). More recent studies have during the last years tested models based on artificial intelligence for determination of net surface radiation for a given location. Geraldo-Ferreira et al. (2011a) and Mahalakshmi et al. (2016a) reported successful estimation of R_{net} by using artificial neural network (ANN) based on meteorological measurements. However, the risk of overfitting increases with fewer observations, and in these situations, statistical regression models are often useful and reliable.

The Land-ATmosphere Interactions in Cold Environments (LATICE) project at the University of Oslo, established an eddy flux tower at Finse in Norway in 2016 to monitor and

evaluate the surface exchange processes between the land and the atmosphere. The establishment of the tower provides important knowledge about the surface energy processes in the low alpine zone. Although the eddy covariance (EC) method is arguably the most accurate and reliable measuring technique for the exchange processes between the atmosphere and terrestrial surface (Finkelstein and Sims, 2001), there are some restrictive conditions for the atmospheric surface layer which must be met for a proper use of this technique. The assumptions include steady state, fully developed turbulence and a flat surface with horizontal homogeneity. For most EC measurement sites these conditions are not fully satisfied. At Finse, an especially large variability of vegetation and topography is challenging for the validity of the measurements. This means, among other things, that the different sizes of the source areas contributing to the measurements of different energy fluxes lead to a mismatch. The nonidentical footprints of the energy measurements is thus a potential cause for the energy imbalance between incoming and outgoing energy, which is observed today.

In 2017, Anders Bryn and Peter Horvath, at the Natural History Museum of the University of Oslo, mapped the nature of one square kilometer around the Finse flux tower based on the Nature in Norway (NiN) system. NiN is a type and description system for all nature types in Norway. Their work resulted in a detailed vegetation map, which corresponds to the area contributing to the energy flux measurements at the Finse flux tower.

The purpose of this study was first and foremost to investigate the effect of non-corresponding footprints between the turbulent fluxes (from EC) and the net surface radiation (from a radiometer) on the energy balance closure at the Finse flux tower. Due to the large variability in surface cover, it was hypothesized that considerable differences in the net surface radiation occurred across the surface. Since the radiometer at the flux tower only provides a one-point measurements of net surface radiation, it was anticipated that these measurements were non-representative for the whole surface cover contributing to the turbulent fluxes. To investigate this, the main objectives of the study were to 1) predict net surface radiation for different surface types and 2) use this information to obtain a more representative value of net surface radiation accounting for the heterogeneity of the surface cover around the flux tower. Spatially distributed measurements of net surface radiation were collected for different surface types based on a classification of the nature types in the vegetation map over Finse. Based on earlier studies with successful estimations of net surface radiation from meteorological variables, linear regression models were fitted, and artificial neural networks trained for predicting continuous time series of net surface radiation for all

the different surface types. The linear model predicted time series were used to derive an overall value of net surface radiation which accounted for the heterogeneity of the surface cover. By doing so, the study intended to estimate a more correct value of net surface radiation which was better comparable to the source area contributing to the turbulent energy exchange than the regular net surface radiation provided by the flux tower.

2 Background

2.1 Surface energy fluxes of an ideal surface

Terrestrial surfaces are continuously interacting with the overlying atmosphere. Through the exchange of energy, CO_2, water and other atmospheric constituents, the earth's surface influences the atmospheric boundary layer above and vice versa. Since most terrestrial surfaces have heterogenous land cover with spatial variability, it is convenient to consider such land cover consisting of a patchwork of individually ideal surfaces (Shuttleworth, 2012). For an ideal surface, illustrated in Figure 2.1, homogeneity across a horizontal patch is assumed. This means that the vertical energy flow across the surface, which is characterized by albedo, thermal emissivity, aerodynamic roughness and the ability to store and capture water in the plant canopy and soil, is equal across the entire surface. The components influencing the surface energy balance, all given with unit Wm^{-2}, are as follows.

The net surface radiation (R_{net}) is the driving input to the surface energy balance. The parameter determines the energy available for physical and biophysical processes, such as evapotranspiration, and soil and air warming of the surface element (Geraldo-Ferreira et al., 2011a). The flux is a net balance of radiant energy over all wavelengths (Shuttleworth, 2012), calculated by the sum of shortwave, S_{net}, and longwave, L_{net}, radiation, i.e.

$$R_{net} = S_{net} + L_{net} = S^{\downarrow} - S^{\uparrow} + L^{\downarrow} - L^{\uparrow} \tag{2.1}$$

Here $S^{\downarrow}$ represents the incoming shortwave solar radiation, while $S^{\uparrow}$ represents the shortwave radiation reflected from the surface, dependent on the surface's albedo. $L^{\downarrow}$ and $L^{\uparrow}$ represents the longwave downward and upward radiation emitted respectively from the atmosphere and the earth surface. In both cases the longwave radiation is dependent on the temperature and emissivity of the emitting spheres. In the used sign convention, the net surface radiation is defined as positive when directed toward the surface. At daytime R_{net} is dominated by the solar radiation, while at night there is typically a negative longwave radiation balance controlling the flux.

As opposed to R_{net}, the sensible heat (H) is defined positive when directed upward from the surface, see Figure 2.1. The parameter represents the transportation of energy between the earth surface and overlying atmosphere when the overlying air is either cooled or warmed in contact with the surface element (Shuttleworth, 2012). The flow of energy is thus dependent on
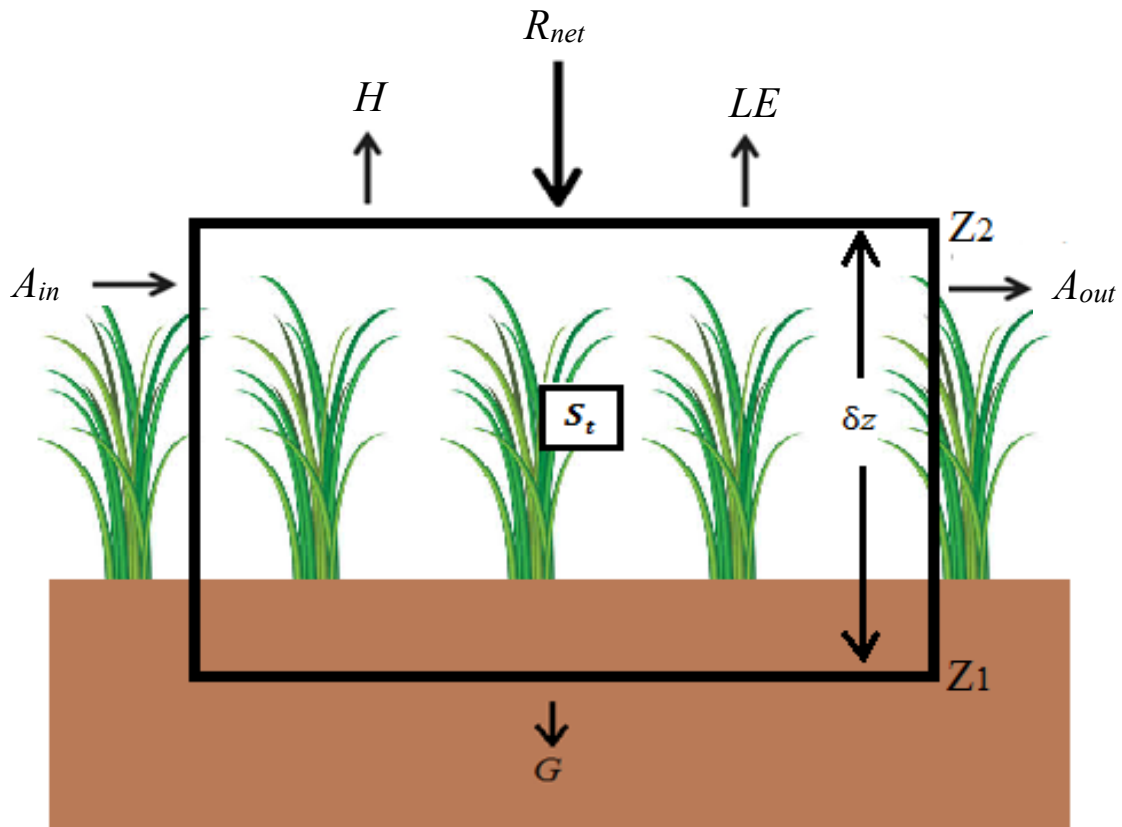
Figure 2.1: The surface energy balance for an ideal terrestrial surface element represented by the fluxes of net surface radiation (R_{net}), sensible heat (H), latent heat (LE), soil heat (G), and horizontally advected energy (A_{in} and A_{out}). S_t represents the energy stored in the surface element by physical storage and biochemical storage. The arrows illustrate the positive direction of the fluxes. All components with units Wm^{-2}. Adapted from Shuttleworth (2012).

both the temperature of the lower atmospheric air and the temperature within the surface element. Typically, at daytime when solar radiation heats the surface, the sensible heat flux is outward, while at night there is a tendency of negative sensible heat fluxes.

The other turbulent flux is the latent heat flux (LE). It describes the energy transfer associated with the phase change of water. For surfaces without snow and ice, the latent heat flux is found as the product of the evaporation rate in kgs^{-1}m^{-2} multiplied by the specific heat of vaporization of water, λ, in Jkg^{-1}. The latent heat transports energy away from the surface during evaporation, while during condensation the energy is transported towards the surface, defined as a negative latent heat flux.

The soil heat flux (G) describes the heat transferred by thermal conduction in the soil. The thermal conduction occurs when the temperature difference between the soil surface and subsurface develops during the day due to the heating of the soil surface from solar radiation (Shuttleworth, 2012). G is typically positive during the day by transferring heat downward, while at night the vertical temperature gradient is positive, which results in a negative soil heat

flux directed toward the surface. Oke (1987) explains the importance of the thermal conductivity and heat capacity for the heat transfer in soils. These thermal properties represent the ability of a soil to conduct heat and the ability of a soil to store heat, respectively. This is dependent on the soil type and the presence of moisture in the soil, and determines how the soil heat flux responds to temperature changes at the surface.

As shown in Figure 2.1, the net advected energy (A_d) is simply calculated by

$$A_d = A_{in} - A_{out} \qquad (2.2)$$

Here A_{in} and A_{out} are horizontally advected energy parallel with the wind, which enters and leaves the surface element, respectively. A_d is defined as positive when bringing energy into the surface element. Most often net advected energy is neglected when investigating the surface energy balance, but in situations with "Oasis effect" (heat advection due to evaporative cooling over a local humid source existing in an arid area), the term may become significant (Oke, 1987).

The term S_t represents the energy stored within the surface element either physically as heat in the ground and canopy, or biochemically through capture/release of energy dependent on photosynthesis/respiration. The physical energy storage between level z_1 in the soil and the reference level z_2 in the atmosphere, shown in Figure 2.1, is typically dependent on the depth δz. For short crops this term is often neglected, while for tall canopies with more biomass and surrounding air, the physical energy storage can become significant (Shuttleworth, 2012). Haverd et al. (2007) reports the importance of the physical energy storage in a forest canopy, by rising the surface energy balance closure from 90% to 101%.

By adapting the first law of thermodynamics to an ideal terrestrial surface (Wilson et al., 2002) and using the sign convention for the fluxes, defined by the arrows in Figure 2.1, the energy balance equation for an ideal terrestrial surface is written as

$$R_{net} - G + A_d - S_t = H + LE \qquad (2.3)$$

The left side of the equation is referred to as the available energy, because these components together define the energy available for the turbulent fluxes of latent and sensible heat during daytime conditions.

2.2   Eddy covariance method

The eddy covariance (EC) method is frequently the most accurate and reliable measuring technique used to measure the exchange of heat, momentum and trace gases between the atmosphere and terrestrial surface (Finkelstein and Sims, 2001). The technique is based on direct measurements of the vertical velocity of the wind and the concentration of the substance of interest by using fast-response sensors in a turbulent flow. When estimating their covariance, it is possible to calculate the vertical flux, with the advantage that no applications of empirical constants are required (Foken, 2008a). However, the method requires some theoretical conditions to be fulfilled. These involve steady state conditions and fully developed turbulence in the atmospheric surface layer, and a horizontal, flat homogenous surface (Foken and Wichura, 1995). Today there are more than 500 long-term operating eddy flux towers around the world as a part of the FLUXNET network. The EC method thus provides a considerable contribution to the study of environmental, biological and climatological controls of the surface exchange between the atmosphere and terrestrial ecosystems (Baldocchi et al., 2001).

To understand how EC is used to calculate the exchange of sensible and latent heat between land and atmosphere, it is fundamental to understand the principle of turbulent mixing. The lowest part of the atmosphere, the atmospheric boundary layer, is normally ~1-2 km thick (Wallace and Hobbs, 2006). The boundary layer is affected by the earth's surface, which generates turbulence. As Bonan (2016) visualizes, the air flow can be represented as consisting of many discrete air parcels, where each air parcel has its own characteristic of temperature and water vapor. The turbulent flow creates eddies, which are irregular and stochastic motions in the air that mix the air parcels either upward or downward (Foken, 2008a). The mixed air transports heat and moisture, dependent on the temperature and water vapor characteristics of the air parcels being mixed.

When observing entities of an atmospheric turbulent flow by using fast-response sensors, it appears that the entities have random, short-period fluctuations from their longer mean value (Wallace and Hobbs, 2006). It is favorable to represent this air flow of a quantity x by a mathematical decomposition of the variable into its time-mean value, $\overline{x}$, and its random fluctuating component, x' (Figure 2.2). This decomposition is known as Reynold's decomposition and is represented as
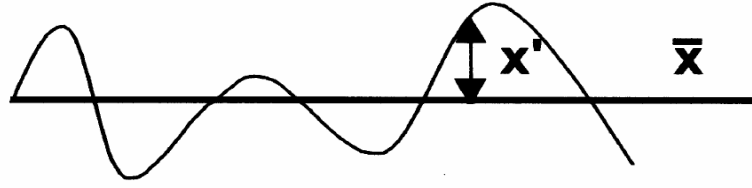
$$x = \overline{x} + x'$$
(2.4)

7

Figure 2.2: Illustration of Reynold's decomposing into mean component and fluctuating component. Figure adapted from Foken (2008a).

For further application of the Reynold's decomposition we require some conditions imposed on the averaging rules, known as Reynold's conditions or Reynold's postulates

$$
\begin{array}{lll}
I & \overline{x'} = 0 & \\
II & \overline{\overline{x}\,y} = \overline{x}\,\overline{y} & \\
III & \overline{x + y} = \overline{x} + \overline{y} & \\
IV & \overline{ax} = a\overline{x} &
\end{array}
\tag{2.5}
$$

Here both x and y are variables, while a is a constant.

The vertical surface flux of a scalar of interest, c, is the product of the vertical velocity of air flow, w, and the scalar (Bonan, 2016). This implies that the mean time-period of the vertical surface flux, is given as:

$$
\overline{wc} = \overline{(\overline{w} + w')(\overline{c} + c')}
\tag{2.6}
$$

$$
= \overline{\overline{w}\,\overline{c} + \overline{w}\,c' + w'\,\overline{c} + w'c'}
$$

$$
= \overline{\overline{w}\,\overline{c}} + \overline{\overline{w}\,c'} + \overline{w'\,\overline{c}} + \overline{w'c'}
$$

$$
\overline{wc} = \overline{w}\,\overline{c} + \overline{w'c'}
\tag{2.7}
$$

Here averaging rules I-III from Reynold's conditions are used. $\overline{c}$ and $\overline{w}$ are the mean value of respectively the scalar of interest and vertical velocity, while c' and w' are the corresponding fluctuating components around their mean values (and themselves have means equal to zero). The scalar flux in eq. 2.7 is just the sum of the transport by mean motion, $\overline{w}\,\overline{c}$, and the transport by turbulence, $\overline{w'c'}$. In the atmosphere a few meters from the ground, the mean transport is generally small (Shuttlewort, 2012; Bonan, 2016). This implies the assumption that $\overline{w}$ equals

0, and the vertical movement of atmospheric entities is entirely dominated by the turbulent flux transport. It is therefore assumed that convergence/divergence of the air flow is negligible. The mean flux reduces to (where N is the number of data points in the sample)

$$\overline{wc} \approx \overline{w'c'} = \frac{1}{N}\sum(w_i - \overline{w})(c_i - \overline{c}) = cov\,(w,c) \tag{2.8}$$

This is the covariance between the vertical velocity and scalar of interest, which represents how the vertical velocity and the concentration of the scalar co-vary. $\overline{w'c'} > 0$ means that air with high density of the scalar of interest is rising and air with low density of the scalar of interest is sinking, therefore having a mean flux transport of the given scalar into the atmosphere away from the ground. Greater covariance implies stronger flux.

The estimated sensible heat flux (H) is calculated from the measured EC between the vertical velocity (w with unit ms^{-1}) and the sonic temperature (T_s in K) as

$$H = \rho_a\,c_p\,\overline{w'T_s'} \tag{2.9}$$

Here ρ_a is the mass density of moist air in kgm^{-3} and c_p is heat capacity at constant pressure of moist air in Jkg^{-1}K^{-1}. Both ρ_a and c_p are based on meteorological measurements from the flux tower (for their calculations, see equations in section 7 in LI-COR, 2017).

By using the measurement of r_{H_2O}, which is the mixing ratio of mole of water vapor per mole of dry air in mmol mol^{-1}, together with the vertical velocity, one finds the EC for the latent heat flux, i.e. $\overline{w'r'}_{H_2O}$. The evaporation rate, F_{H_2O} in 10^{-3}kgs^{-1}m^{-2}, is found by multiplying the covariance with $\frac{1}{v_d}$ and M_{H_2O}, i.e.

$$F_{H_2O} = \frac{1}{v_d}\,M_{H_2O}\,\overline{w'r'}_{H_2O} \tag{2.10}$$

Here, M_{H_2O} is given in kg mol^{-1} and represents the molecular weight of water vapor, which is a constant, and v_d is given in m^3 mol^{-1} and represents the ambient molar volume of dry air. The latter is calculated by

$$v_d = \frac{RT_a}{P_a - e} \tag{2.11}$$

where R is the universal gas constant (8.314 J mol^{-1} K^{-1}) and T_a is averaged ambient temperature in K. e is partial pressure of water vapor in Pa, which is the product of the mole fraction of water vapor per mole of air, X_{H_2O}, and the ambient average pressure P_a in Pa. Both X_{H_2O} and r_{H_2O} are derived directly from the measurements of the tower. Finally, the specific heat of evaporation (λ) given in Jkg^{-1}, which is a function of the ambient air temperature (T_a) is given by

$$\lambda = 10^3(3147.5 - 2.37\,T_a) \tag{2.12}$$

By multiplying the evaporation rate with λ, the estimated latent heat flux (LE in Wm^{-2}) is found as

$$LE = \lambda F_{H_2O} = \lambda \frac{1}{v_d} M_{H_2O} \overline{w'r'}_{H_2O} \tag{2.13}$$

2.3 The energy balance closure problem

The energy balance closure problem arises when the surface energy balance equation (eq. 2.3) is not fulfilled. This means that the incoming energy into a surface element is not equal the outgoing energy and any energy stored in the element. Already during the late 1980s it became obvious that the energy balance at the earth's surface could not be closed with experimental data (Foken and Oncley, 1995). In a comprehensive study performed across 22 sites and 50 site-years in FLUXNET for different ecosystems and climates, Willson et al. (2002) found a general lack of the energy balance closure at most sites, where the mean imbalance was calculated in the order of 20%. It turns out that at most flux measurement sites the sum of turbulent eddy fluxes of the latent and sensible heat is less than the available energy. This is a result of underestimation of turbulent fluxes and/or an overestimation of the available energy. Still, the surface energy balance closure is unsolved for most eddy flux towers, and among several studies it appears that the following reasons are important for the energy imbalance:

1) Systematic measurement errors of the eddy covariance measurements
2) Neglected advection
3) Systematic measurement errors of the net radiation measurements
4) Neglected energy storage and/or incorrect estimation of soil heat flux
5) Mismatching between the source area for the different measurements

To make accurate eddy covariance measurements a careful calibration is crucial. This is obvious, but regular maintenance may become difficult to accomplish when instruments are in the field. The turbulent flux measurements are often exposed for loss of high and/or low frequency (i.e. small eddy/large eddy) contribution to the covariance. The low frequency errors, which increase with the height of the measurements, need to be assessed by evaluating the average time used to measure the covariance (Leuning et al., 2012). At the same time a failure to meet the fundamental assumptions of a homogenous surface with fully developed turbulence and steady state conditions causes important errors one need to consider.

The systematic measurement errors of net radiation measurements cannot be assumed to have a significant effect on the energy imbalance today. This is firstly explained by the tendency of greater underestimation than overestimation, thus not matching the overestimated available energy, and secondly the increase of the accuracy of the radiation measurements during the two last decades (Foken, 2008b). Despite this, evaluating the net surface radiation for heterogenous surfaces in terms of varying land cover and topography may become difficult. Typically, radiation instruments are mounted horizontally, but the strong dependency between the incoming radiation and the slope and aspect of the surface, can cause accurate estimates of the net surface radiation to be difficult to achieve. Especially during daytime in summer months at the northern hemisphere the absorbed radiation at south-facing slopes will differ substantially from a measurement by a horizontal radiometer. To capture the differences of absorbed radiation in a varying terrain, one should therefore consider if the measurements should be performed in a horizontal plane or not. In terms of variation of vegetation and surface cover and varying albedo, one single point measurement of the net surface radiation cannot be considered representative for a heterogenous land surface around a flux tower.

The neglection of energy storage is somewhat important for the closure of the surface energy balance, but the importance of this factor varies depending on the site and type of surface where the measurements are performed. The energy storage is typically large for tall forest canopies. As mentioned in section 2.1.6, the influence of the storage, at least the canopy- and biochemical storage, is generally dependent on the vegetation and its height, and therefore

almost negligible for bare surfaces and short vegetation (Shuttleworth, 2012). However, the physical energy storage in the upper soil layer above the heat flux plate may have a significant influence on the energy balance closure (Foken, 2008b). Since the soil heat flux varies with temperature and depth, the change of energy storage in the soil must be measured to obtain an accurate estimate of the soil heat flux (Leuning et al., 2012). Heusinkveld et al. (2004) report that lack of accounting for the storage term can cause errors in the soil heat flux of 10-200 Wm[-2] for bare soil or sparse vegetation. The fact that the thermal properties for the heat transport is highly dependent on the soil type and the moisture content in the soil may complicate the representation of a representable value for the soil heat flux.

Mismatch of the source areas where the different measurements are performed, can be particularly crucial for the surface energy balance closure at heterogenous surfaces. Figure 2.3 illustrates an eddy flux tower with typical heights for the sensors and their measurements, and the different horizontal scales or footprints of the surface energy components. As opposed to a hypothetical, ideal surface, the energy components are not measured directly at the surface, but either in the air above or in the soil beneath. The measuring height for the net surface radiation is approximately 2 m, and the footprint is in the order of only a few square meters closest to the tower (Foken, 2008b). The soil heat flux plate often covers an even smaller source area. For the turbulent fluxes the sensors are usually installed at an elevation of 2-5 m, and their footprint of the underlying surface may cover up to 200-300 meters in the upwind direction (Foken, 2008b). The nonidentical footprints of the measured surface energy fluxes cause the information used to analyze the surface energy balance to represent different surface covers. This may obviously induce a lack of surface energy balance closure at many sites.

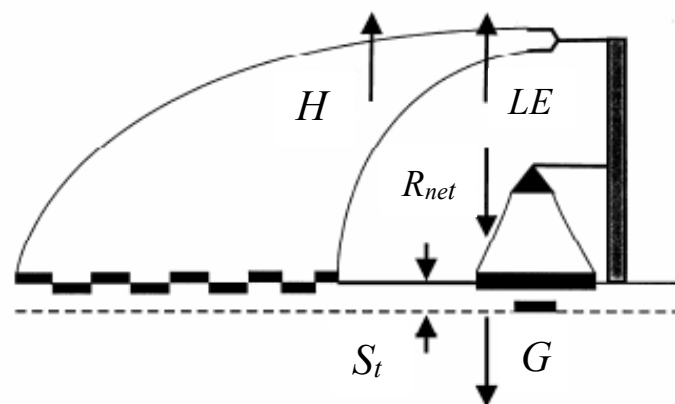**Figure 2.3:** Flux tower, illustrated as the column to the right, with typical measurement height and the horizontal source areas for the different energy fluxes. The cone illustrates the radiation sensor with its footprint, while the left side illustrates the much bigger footprint of the turbulent fluxes. Arrows indicate the positive direction of the fluxes. Figure adapted from Foken (2008a).

2.4　Artificial neural network

An artificial neural network (ANN) is a model developed for information processing inspired by the biological neural network in human beings. By adapting the structure and performance of our biological neural system into machine learning, we develop models to perform pattern recognition tasks. The basic construction of an ANN is the processing units, often called artificial neurons, that are interconnected according to some topology (Yegnanarayana, 1999). The construction of one single processing unit is shown in Figure 2.4. In general, a neuron consists of an activation function and an output part. The activation function receives N numbers of input variables, a_i, where each input value is weighted by a coefficient, w_i. These coefficients are termed synaptic weights and represent the connectivity between the neurons in the network (Geraldo-Ferreira et al., 2011a). The synaptic weights are either described as excitatory, meaning that their sign is positive, or inhibitory, which normally is represented by a negative sign (Gershenson, 2003). Therefore, synaptic weights will either increase or decrease the activation of a neuron. For the multilayer perceptron model, which is one of the classical models for an artificial neuron and the one used in this study, the synaptic weights are adaptive. This means that they are adjustable (Yegnanarayana, 1999). The activation part of the neuron computes a weighted sum from all the weighted input values based on a summing rule and the activation function, φ. This sum, x, often called the activation value, is received by the output part of the neuron, which finally produces a signal to be outputted by the neuron.
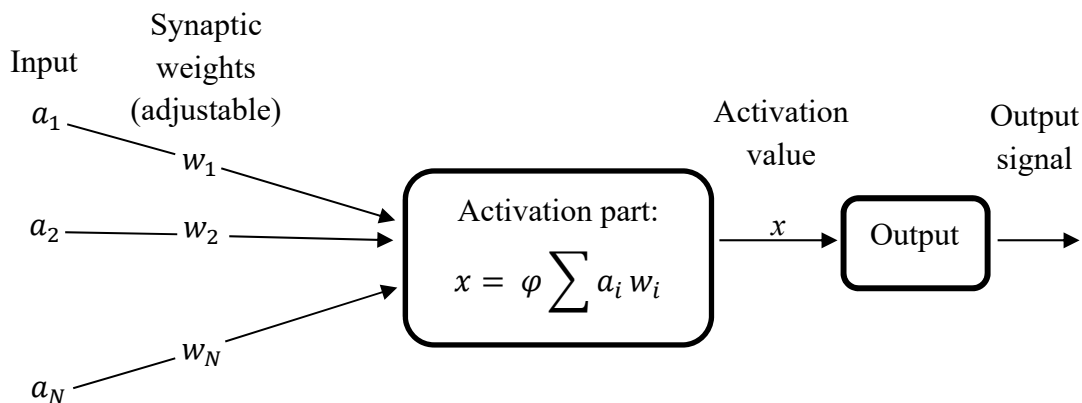

Figure 2.4: Construction of a neuron (processing unit) in an ANN following the perceptron model. Adapted from Yegnanarayana (1999). φ represents the activation function, while $\sum a_i w_i$ illustrates the summing rule. a_i represents input variable i, while w_i represents the weighting coefficient of input i.
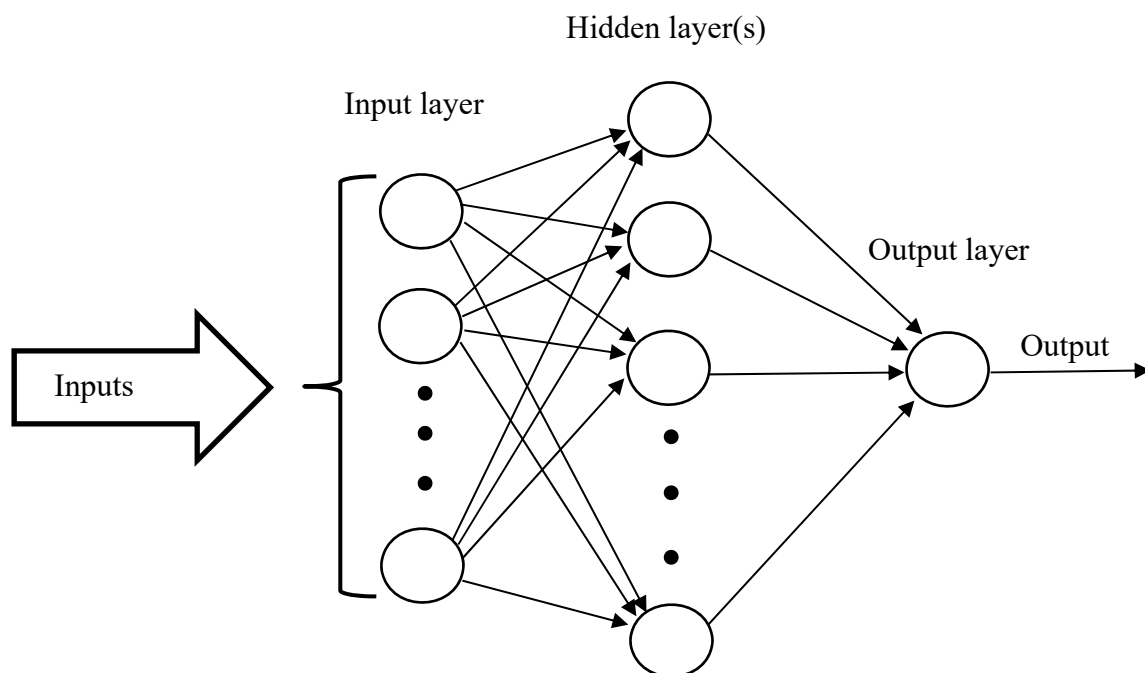
Figure 2.5: Framework of the multilayer perceptron model. Here one circle illustrates one neuron. Adapted from Geraldo-Ferreira, A. et al. (2011b).

The development of a network's topology is crucial for the desired pattern recognition task one wants to accomplish. The topology is explained as the arrangement of the network's processing units, connections and pattern of input/output (Eshwar and Singh, 2012). This means that the neurons should be organized and connected in a suitable manner for the specific task, otherwise the network is useless. A full neural network is put together by connecting many simple neurons together. This is done by grouping neurons having the same activation dynamics and output function together in a joint layer (Yegnanarayana, 1999). In this way, all the neurons in one layer consist of the same processing mechanism and are to some extent similar. In general, an ANN consists of at least three layers, known as the input layer, a hidden layer and the output layer, as shown in Figure 2.5. Sometimes multiple hidden layers are used, where their common characteristic is that their values are not observed in the training set, as opposed to both the input and output layers.

The connections between the different neurons can be made both between processing units within the same layer (intralayer connections) and from a processing unit from one layer to a processing unit in another layer (interlayer connections) (Yegnanarayana, 1999). This implies that the output of one neuron works as the input of another neuron, and neurons may also produce output which is used as input to themselves. For the interlayer connections, the

signals flow either as a feed forward mechanism or as a feedback mechanism. The latter mechanism allows information to flow in both directions, while for feed forward networks, the signal flows only in the direction from the input layer towards the output layer. For a fully coupled multilayer perceptron model, all the neurons in the input layer receive all the different input variables, and all neurons in the hidden layer receive the outputs from all the neurons in the input layer. Based on this architecture, each neuron in the input layer represents a specific characteristic of the input data, and each neuron in the hidden layer represents different functions of the original data by the different weighting. In this way, the different synaptic weighting represents the varying strength of the connections between the neurons, and thus the network has the ability to learn complex non-linear input-output relationships (Eshwar and Singh, 2012).

To develop the ANN to accomplish a specific task, it is necessary to adjust the synaptic weights of each neuron to obtain the desired output from the specific inputs (Gershenson, 2003). This process is known as neural dynamics. In general, neural dynamics consist of two parts, one corresponding to the dynamics of the activation function and the other part corresponding to the dynamics of the synaptic weights (Yegnanarayana, 1999). The activation dynamics determines the activation values of all the neurons for every time unit, and this is followed to recall a pattern stored in the network (Eshwar and Singh, 2012). In addition to storing a pattern in the network, it is necessary to adjust and change the synaptic weights of each neuron. This part of the neural dynamics corresponds to the dynamics of the synaptic weights. By implementing models, known as learning laws or algorithms, an incremental update of the weights will in the end give a useful, desired output from the network. The process is carried out by using training data (a data set where the correct outputs are already known) as input to the network. Then the generated output from the neurons is compared to the desired output by measuring the deviation between the two outputs. The deviation is expressed in terms of the error function or loss function, which is chosen for the specific network. By repetitively updating and adjusting the synaptic weights, the loss function slowly decreases, and the ANN is ready for the desired purpose.

3   Materials and Methods

The work done in the current study is presented schematically in the diagram in Figure 3.1. Each of the different steps will be explained in the following subsections.
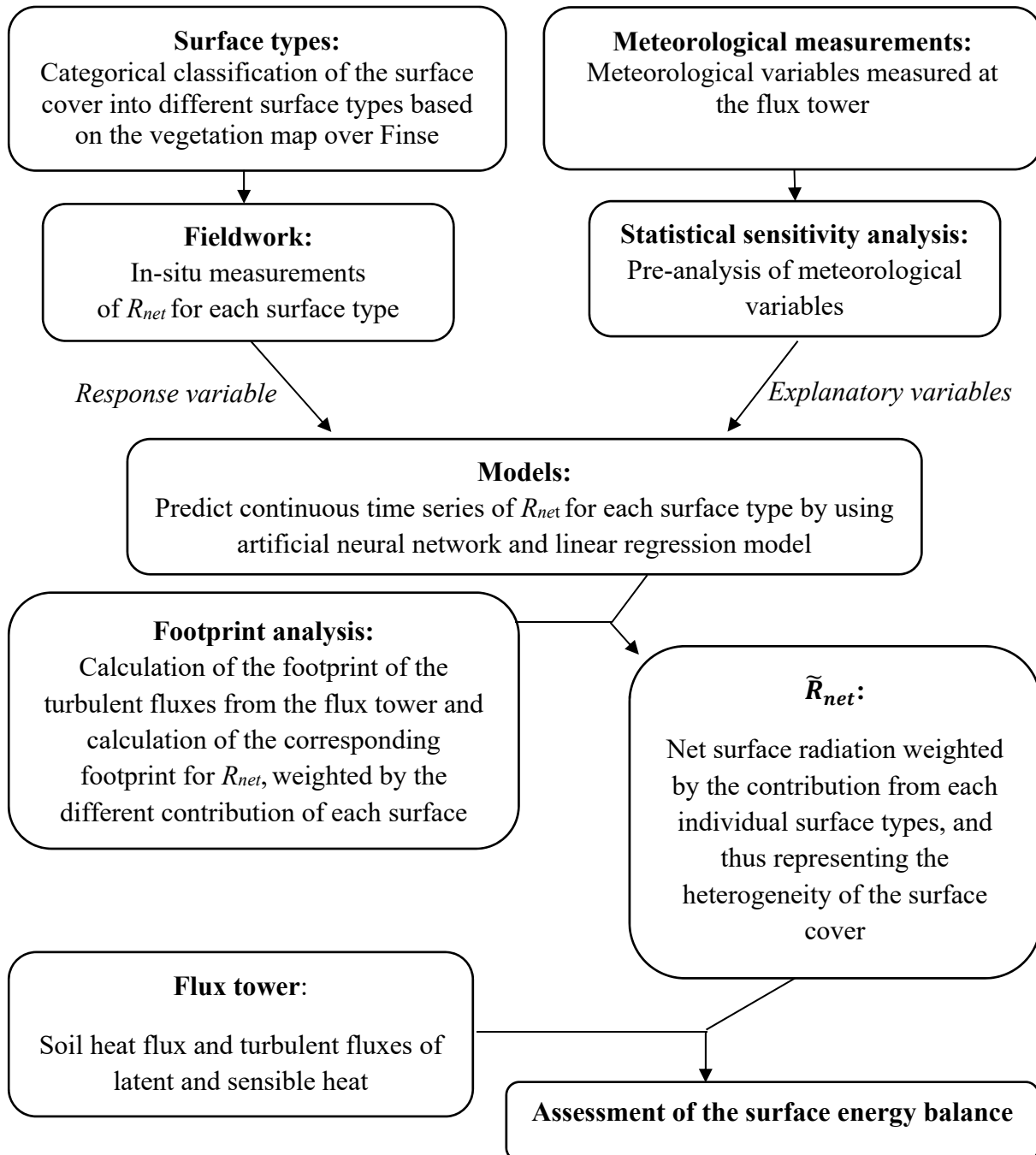
Surface types:
Categorical classification of the surface cover into different surface types based on the vegetation map over Finse

Meteorological measurements:
Meteorological variables measured at the flux tower

Fieldwork:
In-situ measurements of R_{net} for each surface type

Statistical sensitivity analysis:
Pre-analysis of meteorological variables

Response variable

Explanatory variables

Models:
Predict continuous time series of R_{net} for each surface type by using artificial neural network and linear regression model

Footprint analysis:
Calculation of the footprint of the turbulent fluxes from the flux tower and calculation of the corresponding footprint for R_{net}, weighted by the different contribution of each surface

$\widetilde{R}_{net}$:

Net surface radiation weighted by the contribution from each individual surface types, and thus representing the heterogeneity of the surface cover

Flux tower:

Soil heat flux and turbulent fluxes of latent and sensible heat

Assessment of the surface energy balance

Figure 3.1: Diagram showing the different steps in the study. The main objectives were 1) to predict net surface radiation for different surface types and 2) use this information to obtain a more representative value of net surface radiation accounting for the heterogeneity of the surface cover around the flux tower.
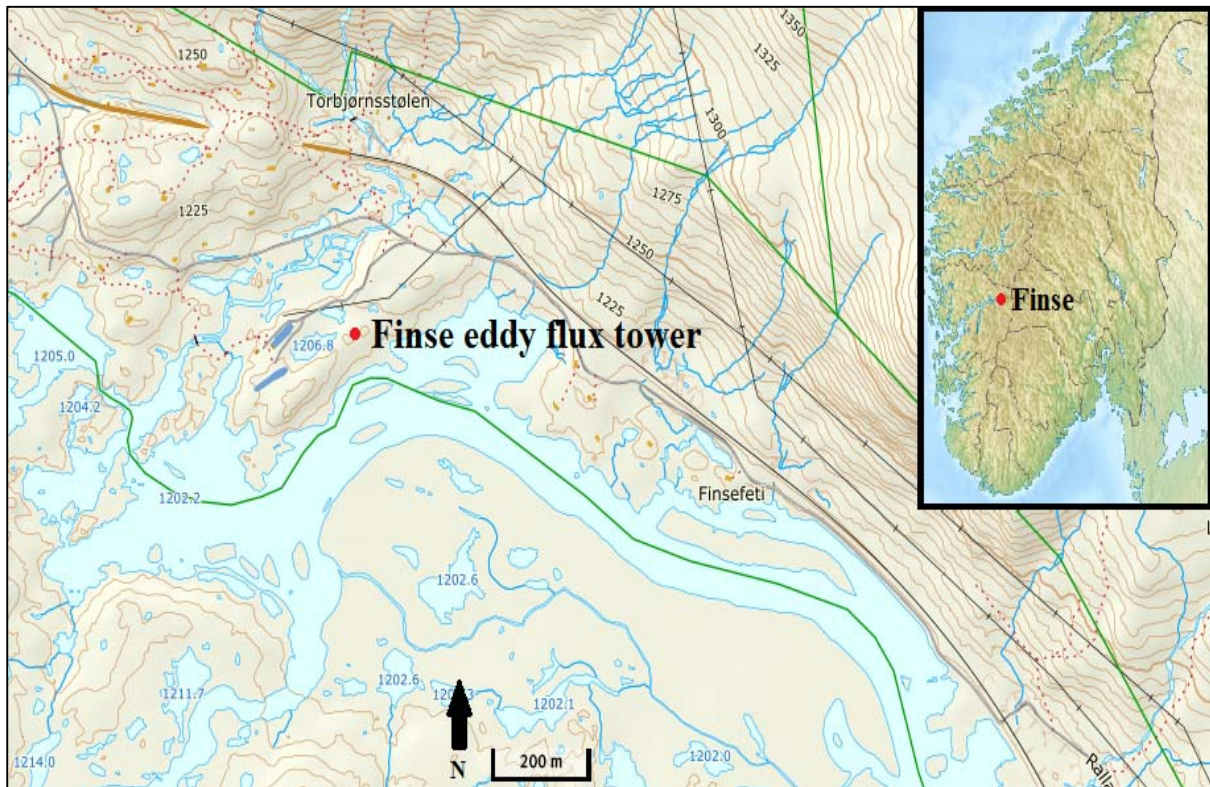
3.1 Site description

Figure 3.2: Location of Finse flux tower. Adapted from Kartverket (2018).

Finse eddy flux tower is located nearby Finse Alpine Research Center (60° 36' N, 7° 30' E) in the southern central Norway (Figure 3.2). The area is found in the northwestern corner of the Hardangervidda mountain plateau, ~1200 m above sea level in the low alpine zone. The Hardangerjøkulen Glacier, with an altitude ~1800 m above sea level, is located southwest of Finse, while in the north we find the Hallingskarvet National Park. Because of Finse's high altitude, the area has an arctic tundra climate. Nevertheless, the climate consists of relatively mild winters, while the summers are cool. This is a result of the transition zone between easterly continental and westerly oceanic climate, where warm, moist westerly winds from the Atlantic Ocean dominate (Leinaas and Schumacher, 2005). The monthly normal temperature for the period 1961-1990 was highest in July with 7.0°C, while lowest in January with -10.1°C. The annual mean temperature was -2.1°C. The cold summer temperature is somewhat explained by the influence of the Hardangerjøkulen Glacier (Leinaas and Schumacher, 2005), where cold air from the glacier tends to sink down to Finse. The normal annual average precipitation for the same period was 1030 mm. The typical low temperatures during summer induce mist and cloud cover, which increase the precipitation in the summer. On the other hand, Finse is occasionally

in the rain shadow behind the Hardangerjøkulen Glacier in events of moist, oceanic southwesterly winds (Gjessing, 1997).

Since the tower is placed in a larger valley, the wind direction distribution in the area is strongly affected by this. The valley extends in the northwest-southeast direction, causing a channeling effect to force the wind to flow along this axis. Therefore, the predominant wind directions are west/northwest and east/southeast. This results in a wide-spread footprint for turbulent fluxes in these directions. The tower is placed on a small ridge running in the northeast-southwest direction, with great variability of topography and surface cover in the surrounding area (Figure 3.3). Closest to the tower the vegetation is dominated by lichens heaths on wind exposed ridges and narrow zones of dwarf shrub heath on the lee-sides. Further downslope, the snow cover increases, and moss snow-beds dominate until the topography flattens out towards the wetlands and river. In the flat areas, water accumulates to generate mires and small ponds. Along the river and streams there are narrow bands of willows (Bryn, n.d).
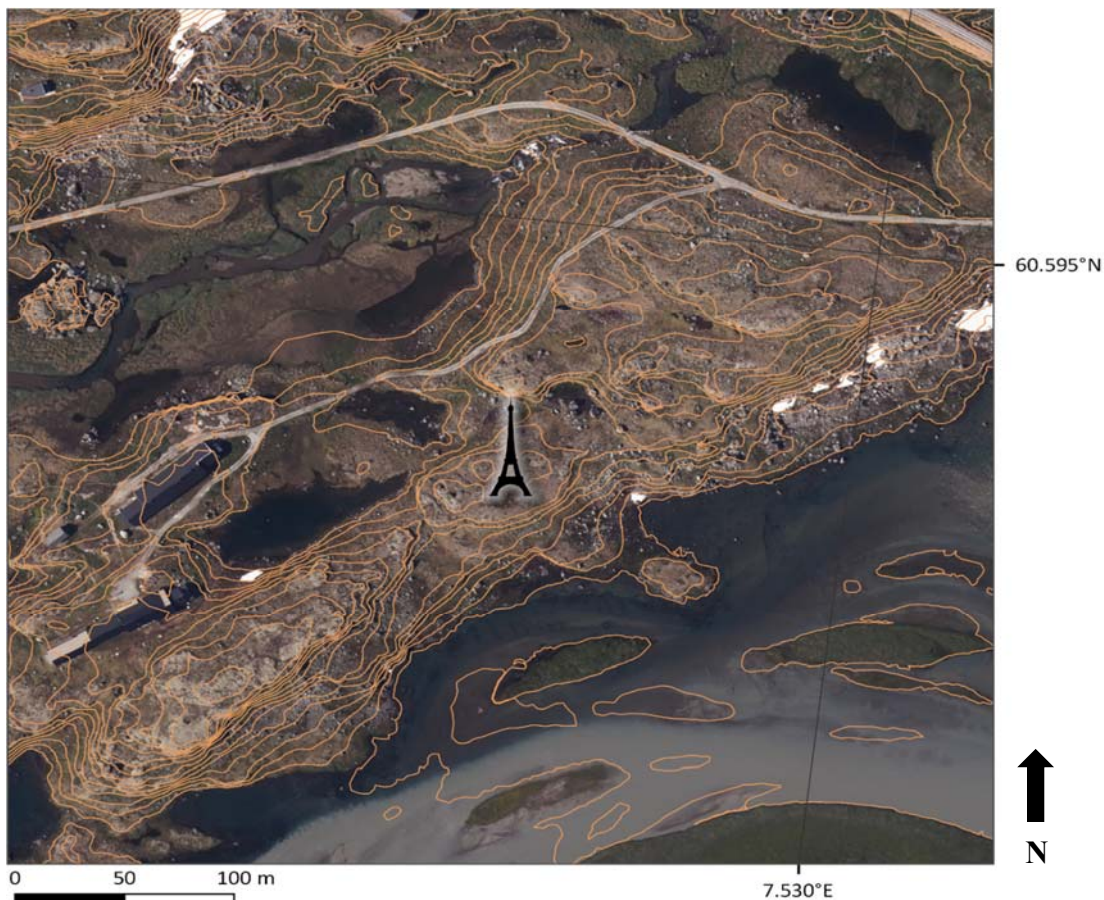

Figure 3.3: Aerial photo with 1 m height contours showing the varying surface cover around the Finse flux tower. Bryn and Horvath (2017).

3.2 Flux tower instrumentation

Figure 3.4: Detailed view of the Finse flux tower. A horizontal boom is installed at an elevation of 4.4 above ground, where the anemometer and the infrared gas analyzer are seen to the right. The radiometer is seen on the left side of the boom (on the southern end).

The flux tower (Figure 3.4) consists of a 10 m tall mast equipped with sensors described in Table 3.1. The net surface radiation is measured by a four-component radiometer, which consists of two pyranometers and two pyrgeometers. The pyranometers take measurements of shortwave radiation both upward and downward and have a spectral range of 300-2800 nm. The field of view is 180 degrees. The pyrgeometers measure the incoming and outgoing longwave radiation and have a spectral range of 4.5-42 µm with a field of view of 150 degrees. The eddy covariance measurements (gas analyzer and 3D anemometer) are sampled with a frequency of 10 Hz, while the other meteorological measurements are sampled at 0.2 Hz. The

EC-system is connected to a flash drive, where the data are stored. The other ancillary meteorological measurements and fluxes from the tower are stored on a Campbell Sci. CR6 logger.

The EddyPro v6.2.0 (LI-COR Inc 2016) software was used to process the raw data from the EC-system at Finse. The analysis and processing from raw data to flux estimates was done automatically after the setup programming, which has been performed by Norbert Pirk. A necessary processing involves checking raw data for instrument errors, coordinate system rotation of wind vector components, extracting turbulent fluctuations from the raw signal, a spectral correction of potential loss of the flux transport for high and/or low frequencies, and a quality control analysis existing of spike filtering and tests to assess the method assumption of steady state and fully developed turbulence. A detailed description of the processing of the meteorological measurements and calculation of fluxes at the Finse flux tower is found in Vatne's (2018) master thesis.

Table 3.1: Instruments installed, and measurements taken at the Finse flux tower. Some sensors are operated by the Norwegian Meteorological Institute (MET).

No.	Instrument	Description	Measurement
1	3D sonic anemometer (CSAT3, produced by Campbell Sci)	Installed at 4.4 m height	Wind speed in three directions and speed of sound (SOS)
2	Closed path infrared gas analyzer (LI7200RS, produced by LI-COR)	Installed at 4.4 m height	Concentration of H_2O and CO_2
3	Four-component radiometer (CNR4 net radiometer, produced by Kipp & Zonen)	Installed at 3.5 m height	Net surface radiation
4	Two soil heat flux plates	Installed ~0.1 m below surface and 0.5 m from each other	Soil heat flux
5	Air temperature sensor (MET)	Installed at 10 m and 2 m height	Air temperature
6	Relative humidity sensor (MET)	Installed at 10 m at 2 m height	Relative humidity
7	2D ultra sonic wind anemometer (MET)	Installed at 10 m height	Horizontal wind component
8	Infrared thermometer (MET)	Installed at 4.4 m height	Surface temperature
9	Barometer (MET)	Installed at 2 m height	Air pressure

3.3   Classification of the surface cover into different surface types

During 2017, Anders Bryn and Peter Horvath mapped the vegetation of the area of one square kilometer around the Finse flux tower by using the Nature in Norway (NiN) system. NiN is a full coverage system that describes all nature variation in Norway. The high-resolution vegetation mapping at Finse made it possible to characterize the footprint of the flux tower from the vegetation. This knowledge is important for understanding which types of vegetation and surface covers that contribute the most to the measurements of the turbulent fluxes by the tower. The vegetation map for Finse consists of 32 different nature types and is shown in Figure 3.5.

Before in-situ measurements of net surface radiation could be performed during field work, it was necessary to do a categorical classification of the land surface at Finse by categorizing nature types with similar structure and albedo into new, joint surface types. This was necessary to achieve a sufficient number of measurements within each surface type during the time available for field work and to ensure that the footprint of the radiometer used for the measurements was approximately on the same order of magnitude as the extent of the patches of the different surface types. This adaption ensured that net surface radiation was only being measured for one surface type at a time.

The categorical classification was performed in collaboration with Anders Bryn and Peter Horvath, where the classification was mainly based on the main type (i.e. T01, T03, V1, V4 etc.) of the nature types, with some exceptions. A classification based on the main types implied that nature types with approximately similar albedo were classified into the same surface type. At the same time, nature types with the same vegetation structure, vegetation function and the same access of water were grouped into the same surface type. The different surface types were therefore representing different regimes of biological productivity and different ability to store and capture precipitation. These are important factors that control the heat balances within the different surface types, which is vital for the emissions of longwave radiation. The classification resulted in 11 new surface types numbered from 0-10. In Table 3.2, all the nature types are described. The far-left column in the table describes which surface type each nature type has been classified into. Surface type 0, which consisted of nature type T35-C1, T35-C2 and T39-C4, have been ignored in this study, since this surface type is strongly affected by human activities (buildings and gravel roads) and was therefore not of interest.

By using the geographical information system ArcMap, a new layer containing the 11 surface types was derived from the vegetation map. This was done by merging the area of all the nature types that belonged to the same surface type. The area of each surface type was

calculated to detect how large area the different surface types constitute of the land cover around the flux tower. Surface types 2, 8 and 9 were found to only account for 1.07%, 0.21% and 1.74%, respectively, of the total mapped area around the tower. Due to their insignificant contributions to the flux tower's footprint, these surface types were excluded from the fieldwork and the study. The remaining seven surface types investigated in this study are shown in the surface type map in Figure 3.6.

Surface type 1 consisted of open water ecosystems and was found as open ponds north-west of the tower and as the river running south-east of the tower. Surface type 6 consisted of open flood plain on coarse sand and rock found along the river and smaller streams. Surface type 3, 4 and 7 represented vegetation of lighter lichen on ridges, mountain heathlands on the lee sides, and fens, respectively. Surface type 5 consisted of snow beds and boulder fields, while surface type 10 consisted of late and extreme snow beds. Photos shown in Figure 3.7 illustrate typical characteristic of each of the seven surface types.
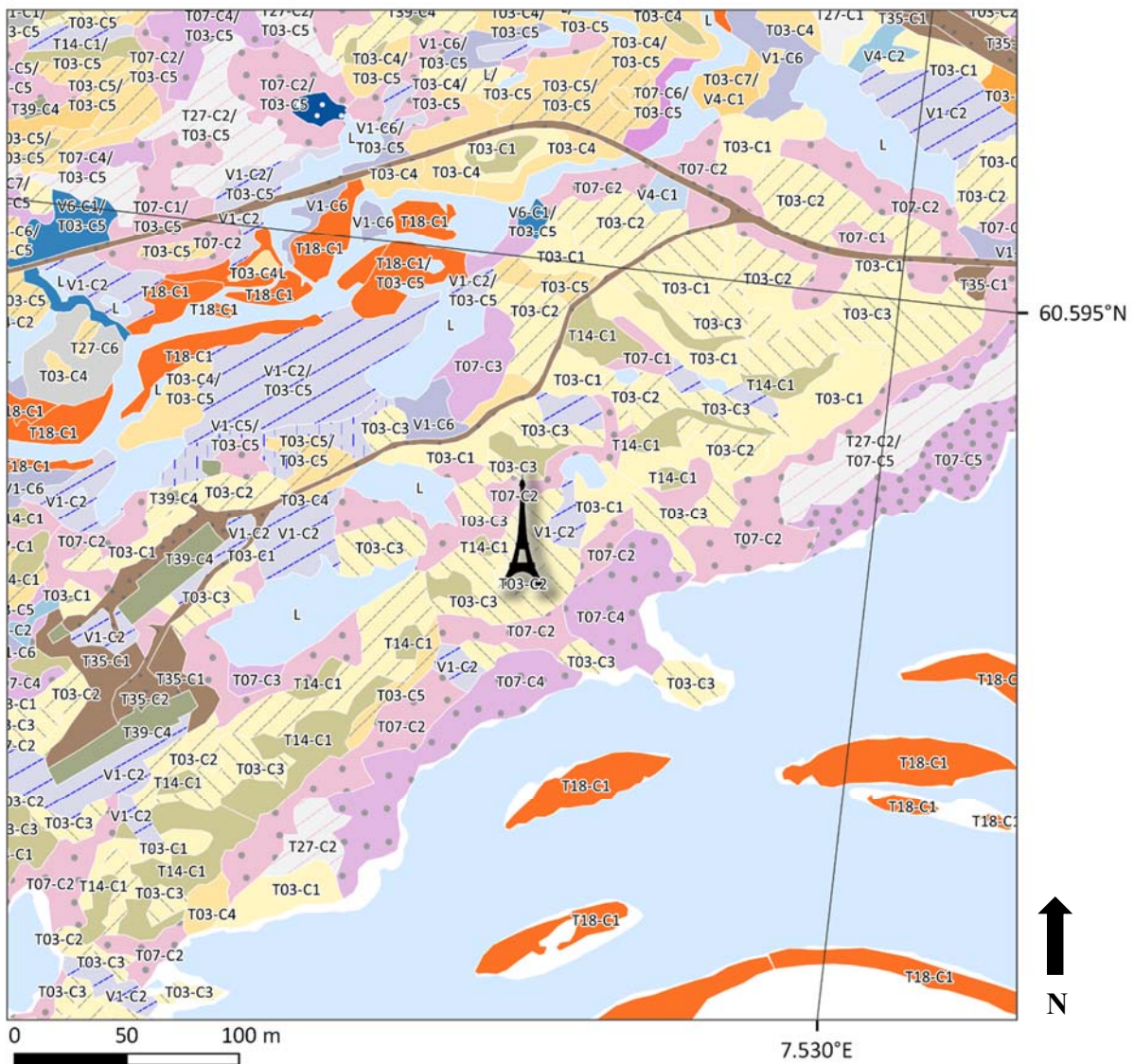
Figure 3.5: Vegetation map for the Finse flux tower. The nature types are described in Table 3.2. Mapped by Horvath and Bryn (2017).

Table 3.2: The 32 nature types with their descriptions, which are mapped at the Finse flux tower. The column to the far left numerates which surface type each nature type was classified into. The second column describes typical surface characteristic, and the terminology used, for the surface types that were investigated in this study.

Surface type	Surface characteristic	Nature type	Description
0		T35-C1	Strongly modified loose soil
		T35-C2	Strongly modified loose gravel and sand
		T39-C4	Strongly modified hard inorganic substrates
1	Water	L	Limnic benthic ecosystem
2		T01-C1	Drought-resistant lime-poor rock
		T27-C1	Lime-poor and intermediate boulder field
		T27-C6	Lime-poor and intermediate ridge-like boulder field
3	Lichen-heathlands	T03-C3	Lime-poor mountain lichen-heathlands
		T03-C6	Intermediate mountain lichen-heathlands
		T14-C1	Lime-poor and intermediate ridge
4	Mountain heathlands	T03-C1	Lime-poor lee side
		T03-C2	Lime-poor mountain heathlands
		T03-C4	Intermediate lee side
		T03-C5	Intermediate mountain heathlands
		T03-C7	Slightly lime-rich lee side
5	Moderate snow beds	T07-C1	Very lime-poor moderate snow bed
		T07-C2	Slightly lime-poor moderate snow bed
		T07-C3	Intermediate moderate snow bed
		T07-C6	Slightly lime-rich moderate snow bed
		T07-C12	Intermediate spring-water-influenced snow bed
		T27-C2	Lime-poor and intermediate snow-bed boulder field
		V6-C1	Lime-poor and intermediate moderate wet snow bed
		V6-C7	Lime-poor and intermediate late wet snow bed
6	Flood plains	T18-C1	Open flood plain on coarse sand and rock
7	Fens	V1-C2	Lime-poor open fen
		V1-C5	Very lime-poor open fen margin
		V1-C6	Lime-poor open fen margin
8		V4-C1	Fairly lime-poor and intermediate spring
		V4-C2	Moderately lime-rich spring
9		T03-C13	Intermediate tall-herb mountain meadow
10	Late snow beds	T07-C4	Intermediate late snow bed
		T07-C5	Intermediate extreme snow bed
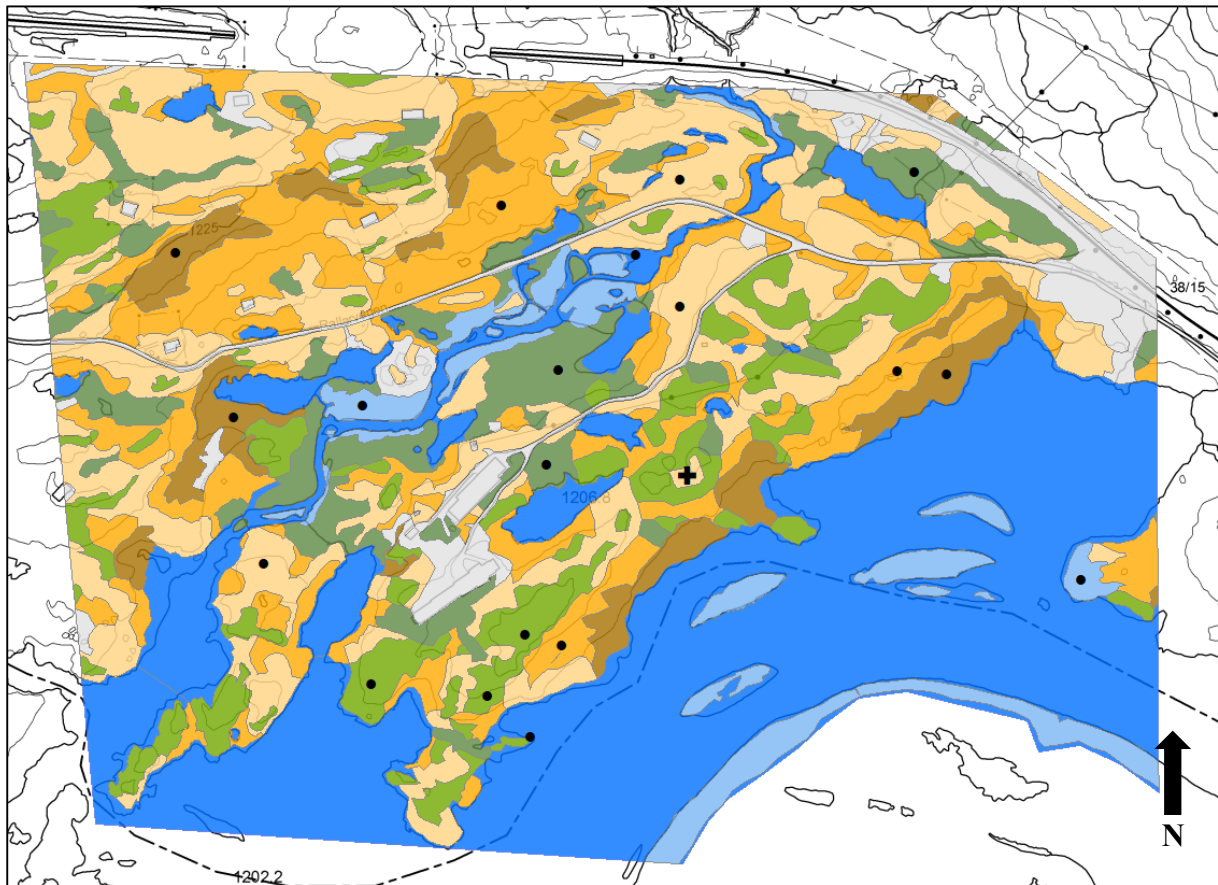
Figure 3.6: Surface type map showing the seven final surface types that were investigated in the study. The classification of each surface type was based on the nature types in the vegetation map in figure 3.5. For an explanation of the different surface types, see Table 3.2. The grey regions show the area of surface type 0, 2, 8 and 9, which were excluded from the study. The black cross displays the location of the Finse flux tower. The black dots show the location of the measuring points where the mobile radiation tower was placed during fieldwork.

Figure 3.7: An overview showing typical surface characteristics of the seven different surface types where net surface radiation was measured; (a) surface type 1: water, (b) surface type 5: moderate snow beds, (c) surface type 3: lichen-heathlands, (d) surface type 6: flood plains, (e) surface type 7: fens, (f) surface type 4: mountain heathlands, and (g) surface type 10: late snow beds.

3.4   Fieldwork

The in-situ measurements of net surface radiation of the different surface types were performed in the period 18.08.18 to 25.08.18. In advance of the fieldwork, a mobile radiation tower was built specially for the current study. In this way, necessary equipment for the measurements was easily moved around between the different surface types. The tower is shown in Figure 3.8. It consists of a CNR1 four-component radiometer (produced by Kipp&Zonen), which was connected to a CR6 datalogger (produced by Campbell Scientific). A motor cycle battery connected to the datalogger worked as power supply. The net surface radiation was sampled with a sampling frequency of 0.2 Hz, before the measurements were estimated to half-hourly fluxes. The four-component radiometer have the same sensor properties as the four-component radiometer of the stationary flux tower described in section 3.1.2. The manufacturer of the net radiometer suggested that the radiometer should be mounted at a height of at least 1.5 m above ground, but this height was found to capture measurements from a spatial scale larger than most of the extent of the patches of the different surface types. A mounting height of 1.1 m was therefore chosen as a compromise to ensure that the radiation was measured only within the same surface type at a time and to minimize shading effects of the instruments on the surface. In addition, the tower became more stable and sturdier when the radiometer was installed at a lower elevation above ground.

Based on the seven surface types, two to three measuring points within each surface type were selected. This was done to consider the variation of the surface cover within each surface type and to consider the varying topography in terms of differences in aspect and slope of the terrain, which may impact the radiation balance at place. Since 99% of the outgoing radiation from the surface is measured for a circular area of radius 10 times the measurement height (Kipp&Zonen, 2002), the patches with the largest extent of each surface type were chosen as suitable measuring points. The black dots marked on the surface type map in Figure 3.6 show the selected measuring points.

During the fieldwork the tower was placed at a measuring point for four hours at a time before it was moved to the next measuring point. This procedure was performed during daytime from 8 am to 8 pm. While during night time, from 8 pm to 8 am, the tower was measuring at the same measuring point. By following this procedure, it was possible to do measurements within each of the seven different surface types evenly distributed throughout the whole period of the fieldwork. This procedure also assured that all surface types were represented by at least one measurement from all times of the day. When the tower was placed at a measuring point in

field, a compass was used to ensure that the radiometer always pointed to the south. Due to uneven and non-horizontal surfaces at some measuring points, the radiometer was sometimes placed parallel to the surface instead of horizontally.

(a)

(b)
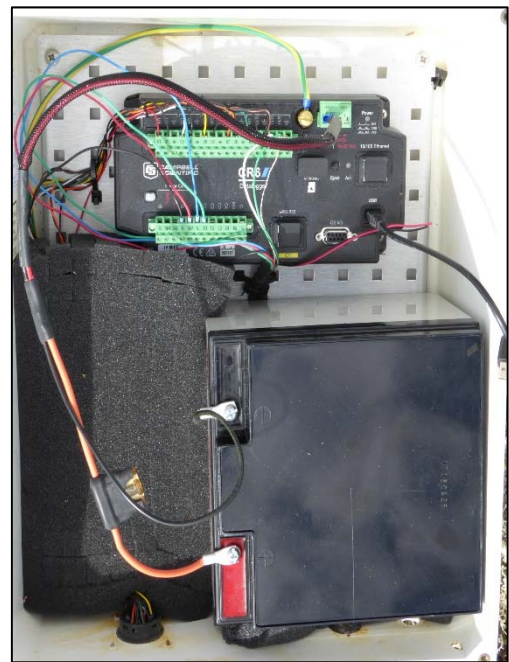
(c)

Figure 3.8: Photos showing the mobile radiation tower (a) used for measuring net surface radiation for the different surface types. A CNR1 four-component radiometer (b) was connected to a CR6 datalogger and a power supply (c).

3.5 Predicting net surface radiation by using linear regression model

In this study, linear regression models (LMs) were used to provide continuous time series of net surface radiation for the different surface types investigated. LMs have been widely used to predict net surface radiation based on meteorological parameters (Geraldo-Ferreira et al., 2011a; Mahalakshmi et al., 2016; Iziomon et al., 2000; Kjaersgaard et al., 2007). However, the predictions of various regression models are dependent on the local fitting of the regression coefficients, which implies that regression models are dependent on the surface type and its meteorological conditions, thus only valid for a restricted area. According to Kjaersgaard et al. (2007), the two most commonly used linear regression models for predicting net surface radiation are simple models with either incoming shortwave radiation, or both albedo and incoming shortwave radiation as explanatory variables. In the current study, measurements of incoming longwave radiation were also provided. Three different models were tested: a simple model with only incoming shortwave radiation as explanatory variable, a second model with both incoming shortwave and longwave radiation as explanatory variables, and a third model with incoming shortwave and albedo as explanatory variables. The best model found for predicting R_{net} for the different surface types was

$$R_{net} = \alpha + \beta_1 * S^{\downarrow} + \beta_2 * L^{\downarrow} + \varepsilon \qquad (3.1)$$

Here α, β_1 and β_2 are regression coefficients, while $S^{\downarrow}$ and $L^{\downarrow}$ represents the incoming shortwave and longwave radiation, respectively. ε represents the error term, which is assumed to be uncorrelated and normally distributed with expectation zero and constant variance. The in-situ measurements of net surface radiation for each surface type were used together with the measured $S^{\downarrow}$ and $L^{\downarrow}$ by the mobile radiation tower for fitting individual regression models for each surface type. Then continuous times series of R_{net} were predicted for each surface type by using the individual fitted regression coefficients, equation 3.1 and the data of continuous measured $S^{\downarrow}$ and $L^{\downarrow}$. The accuracy of all the models were assessed through the coefficient of determination (R^2) and the root mean square error (RMSE). The coefficient of determination indicates the quality of the fitted model by quantifying how much of the variation in R_{net} that is explained by the models for the different surface types. RMSE is a measure of how well the different estimated models fit to the observed data.

Since only a small number of in-situ measurements of R_{net} were collected for each surface type during fieldwork, all the measured data were used as training data for fitting the

linear regression models. In the absence of test data, a cross-validation for each of the linear regression models was performed to further assess their suitability as predictive models. Here, a leave one out cross validation (LOOCV) was conducted. The LOOCV is an extreme case of the leave-p-out-cross-validation, but still frequently used to assess how good a statistical model is when it is generalized to independent data. The technique is thus a valuable indication for the accuracy of the regression models for the different surface types. The LOOCV is performed by computing the root mean square error prediction (RMSEP) by the following procedure: for every i'th iteration, the i'th observation is excluded when fitting the linear model, then the i'th observation is used for obtaining the prediction error. After repeating the procedure for all observations, the RMSEP is calculated as the square root of the average of the squared prediction errors. As a corresponding measurement to R^2, the coefficient of determination for prediction (R^2_{pred}) based on the LOOCV was calculated to measure how well the LMs predicted net surface radiation based on new, independent observations of incoming shortwave and longwave radiation.

3.6 Predicting net surface radiation by using artificial neural network

3.6.1 Selection of input variables

A prerequisite for developing an artificial neural network (ANN) fitted for a specific pattern recognition task, is to carefully select input and output variables to the network. Since an ANN is a model developed after the selection of input variables, a strong relationship among the predictors and the response is crucial, and output data must be influenced by changing input variables (Caner and Kecebas, 2011). According to this, a sensitivity analysis was performed for the meteorological variables measured at the Finse flux tower. This was done to; (i) find the strongest relationships between the output variable R_{net} and the other meteorological input variables, to (ii) assure that variables with little or no predictive power were removed and to (iii) examine potential correlations between the input variables. A selection of input variables is thus important for avoiding noise and disturbances, potential overfitting, and multicollinearity and redundancy among the data. Based on a successful estimation of R_{net} by using ANN reported by Geraldo-Ferreira et al. (2011a) and Mahalakshmi et al. (2016a), the meteorological data investigated in the statistical sensitivity analysis were air temperature (AT), relative humidity (RH), wind direction (WD), wind speed (WS), shortwave incoming radiation ($S^\downarrow$) and longwave incoming radiation ($L^\downarrow$). All the measurements were collected at the Finse

flux tower, except the incoming radiation. Due to a technical error with the upward looking pyrgeometer at the Finse stationary flux tower, which resulted in wrongly measured incoming longwave radiation, the incoming radiation was provided by the mobile radiation tower instead of the stationary flux tower. However, all incoming radiation is assumed to be homogenous for an area corresponding to the size of the study area at Finse. This means that the incoming radiation measured by the stationary flux tower should equal the radiation measured by the mobile radiation tower. The data were collected in the period of 18.08.2018 – 25.08.2018.

3.6.2 Training process and model evaluation

Based on the statistical sensitivity analysis of the meteorological variables, it was decided to train two different artificial neural networks. In the first neural network (NN1), all the meteorological variables ($S^\downarrow$, $L^\downarrow$, AT, RH, WS and WD) were used as input variables. In the second neural network (NN2), all variables, except the incoming radiation, were omitted. This was done to investigate how a reduction of the input variables affected the predictive power of the neural networks.

The package neuralnet in R was used for developing both NN1 and NN2. This is a package built for training models concerning regression problems. Neuralnet is a multilayer perceptron model (MLP) where the synaptic weights are adaptive, organized in a feedforward mechanism with only intralayer connections. In this study the resilient backpropagation with weight backtracking (RPROP+) learning algorithm was chosen when training the network. This was chosen as the learning algorithm due to its rapidity when training neural networks for regression problems (Günther and Fritsch, 2010). The training algorithm RPROP+ is similar to the traditional backpropagation algorithm, but with the advantage that a separate learning law, which can change during the training process, is included for each weight. Thus, the network uses a learning rate which is appropriate for the whole training process and the entire network (Günther and Fritsch, 2010). The network is trained by comparing the given output of R_{net} from the data to the predicted output of R_{net}, and then an error function is calculated. For every time this procedure is repeated, the synaptic weights are adjusted to find the local minimum of the error function. This implies that the error slowly approaches convergence. In this study, the neural networks were trained with the sum of squares (SSE) as error function, while a threshold value of 0.01 was used as stopping criterion. The activation function was chosen to be logistic, which required that a normalization of the data was necessary before training could be performed.

In addition to considering the input variables, the selection of the architecture with the right numbers of layers and neurons is crucial for developing a successful predictive model. The optimal number of hidden layers and neurons is problem specific. This depends on more factors, such as the number of input and output variables, training data available, the complexity of the problem, the training algorithm used, and the function to be learned. A neural network with a complex architecture consisting of too many hidden layers and neurons, will most probably not learn the underlying statistical properties of the data, but rather overfit to the training data. An architecture that is too simple will result in a network that fails to work as a predictive model due to poor signal representation of the dataset.

According to this, a more extensive model selection was performed by training and comparing many different models. Due to the small dataset of observations of net surface radiation for every surface type, all the collected data was used for training the neural networks. For all the seven surface types, and for both NN1 and NN2, one single hidden layer neural network with the number of neurons varying from one to six were trained. Then neural networks with two hidden layers with the number of neurons in the first layer varying from one to six and the number of neurons in the second layer varying from one to three, were trained. For all different combinations of hidden neurons, the RMSE for fitting the models were calculated. In the absence of test data, a LOOCV was performed for calculating the prediction RMSE for all the different models. For every surface type, the model with the lowest RMSEP and RMSE was selected for predicting the net surface radiation. In Table 3.3, the final models used in predicting R_{net} for the different surface types are shown.

Based on the individually trained neural networks for every surface type, continuous time series of net surface radiation were predicted by using the continuous measurements of incoming shortwave and longwave radiation as input variables. The accuracy of all the models were assessed through the coefficient of determination (R^2) and coefficient of determination for the prediction (R^2_{pred}) from LOOCV.

Table 3.3: The neural networks used for predicting net surface radiation for each of the different surface types. The networks are selected based on the RMSEP and RMSE from the model evaluation process.

Surface type	Input variables	# Neurons in the first hidden layer	# Neurons in the second hidden layer
1: Water	$S^\downarrow, L^\downarrow$	2	0
3: Lichen-heathlands	$S^\downarrow, L^\downarrow$	2	3
4: Mountain heathlands	$S^\downarrow, L^\downarrow$	4	0
5: Moderate snow beds	$S^\downarrow, L^\downarrow$	5	0
6: Flood plains	$S^\downarrow, L^\downarrow$	6	0
7: Fens	$S^\downarrow, L^\downarrow$	2	0
10: Late snow beds	$S^\downarrow, L^\downarrow$	1	0

3.7 Comparison of net surface radiation for the different surface types

The predictions provided by the linear models of net surface radiation for the different surface types were compared by performing an analysis of covariance (ANCOVA). This was done to investigate whether there was a significant effect of the surface characteristics affecting the net surface radiation between the different surface types. Since the main purpose of the ANCOVA was to test if there was an overall difference between the different surface types, it was not tested explicitly whether there was a significant difference between the α's or β's fitted in the different models. If a statistical difference was detected, it meant that there was a significant difference in albedo and/or properties for emissions of longwave radiation between the surface types.

The comparison was performed by pairwise analysis of two and two surface types. First, a categorical variable (dummy variable) representing which surface type the measurement belonged to, was added to the dataset. Then a model consisting of incoming shortwave radiation, incoming longwave radiation, the categorical variable and the interactions between the categorical variable and the continuous radiation variables, was fitted. This model was called the full model. Then a similar model, but where the categorical variable and its interactions were omitted as predictor variables, was fitted for the same dataset. This model was called the reduced model. By doing a partial F-test of the full and reduced model, it was revealed whether the categorical variables should be included or not. If a significant contribution from the categorical variable was found, it meant that there was a statistically significant difference in net surface radiation between the two surface types tested against each other. 21 different partial F-tests were performed to compare all the seven surface types against each other. The test statistic was set to a level of significance of 1 %. A 1% level was considered

as conservative, and was therefore chosen as a Bonferroni-like (Miller, 1981) compensation for the increased probability of erroneous rejection of the hypothesis of no difference between the surface types when several tests were performed on the same data.

3.8 Footprint analysis

To characterize the footprint of the flux tower from the different surface types, it was necessary to perform a footprint analysis. The footprint of the turbulent fluxes may be visualized as the horizontal source area of the upwind direction of the surface containing effective sources and sinks contributing to the measurement point (Kljun et al., 2002). The footprint calculations averaged over a longer measurement period, is known as the footprint climatology. For a given measurement height of the EC system, the footprint is dependent on the wind speed, wind direction, turbulence intensity and atmospheric stability. The wind speed and direction are particularly important when determining the footprint area for a heterogeneous surface cover. The turbulence intensity and atmospheric stability are influenced especially by the variation of the topography and surface elements. The footprint of the EC system was derived by using the Flux Footprint Prediction (FFP) online data processing, where the method of estimation is given by Kljun et al. (2015). The measurement height above ground was set to 4.4 m and the displacement height was set to 0. In addition to this, the coordinates of the flux tower, wind speed, wind direction, friction velocity, Obukhov length and the standard deviation of lateral velocity fluctuations after wind component rotation, were needed. These parameters were derived from the EC measurements from the flux tower. The footprint climatology was calculated with half-hour input data from the period 18.08.18 - 25.08.18.

The calculation of the footprint climatology was outputted as two-dimensional raster data from the online processing. These data were assigned to the surface type map by using a linear transformation in ArcMap. The area of each surface type within the turbulent footprint climatology was then calculated to detect the percentage contribution, p_i, from each of the different surface types. The weighted value (when assuming a uniform weighting among the different surface types within the area corresponding to the footprint climatology) of net surface radiation, $\tilde{R}_{net}$, were found by

$$\tilde{R}_{net} = \sum_i p_i * R_{net,i} \qquad (3.2)$$

Here $R_{net,i}$ represents the net surface radiation from surface type i = 1, 3, 4, 5, 6, 7 and 10. $\tilde{R}_{net}$ thus represents the corrected value which takes the heterogenous surface cover around the flux tower into account. In this way, the non-corresponding footprints of the turbulent energy fluxes and the net surface radiation are corrected. However, the assumption of uniform weighting among the different surface types is a simplification. Different locations and surface types may have different weights.

3.9   Assessment of the energy balance closure

The energy balance closure was investigated for the period 18.08.2018 – 25.08.2018. This was done by calculating the energy balance ratio (EBR) and by performing an ordinary least squares (OLS) regression between the turbulent fluxes ($H + LE$) as the response variable and the available energy ($R_{net} - G$) as the predictor variable. A perfect energy balance evaluated with the OLS regression implies an intercept of zero, and coefficient of determination and slope of the regression line equal to one. This method assumes that there are no random errors in the independent variables of R_{net} and G, which is a simplification (Majozi et al., 2017).

The energy balance ratio was found by calculating the ratio of the sum of turbulent fluxes of latent heat (LE) and sensible heat (H) to the sum of available energy of net surface radiation (R_{net}) and soil heat flux (G), i.e.

$$EBR = \frac{\sum (LE+H)}{\sum (R_{net}+G)} \tag{3.3}$$

The ideal closure is reached if EBR equals one. This method allows us to evaluate the energy balance at longer timescales by averaging over random errors in the half-hour measurements from the eddy flux tower. It will also tend to remove systematic effects, like the tendency of overestimated daytime fluxes and underestimated nighttime fluxes (Majozi et al., 2017).

In both methods the energy balance closure was investigated with the measurements of R_{net} measured by the tower, in addition to the footprint corrected value of net surface radiation, $\tilde{R}_{net}$, provided by the predictions from the LMs.

To assure that the measurements of the turbulent fluxes used for evaluation of the energy balance closure were of high quality, all the half hour estimates without the highest

measure of quality, i.e. turbulent flux estimates with quality flag 1 or 2, were discarded. Also, the half hour estimates of the turbulent fluxes where the mean wind speed was less than 2 ms^{-1} were discarded. This was done to ensure that the assumption of well-developed turbulence was fulfilled.

4 Results

4.1 Meteorological data

4.1.1 Meteorological conditions

Numerical statistics of meteorological variables measured for the period 18.08.2018 – 25.08.2018 at the Finse flux tower are shown in Table 4.1. The incoming radiation and the net surface radiation are also included in the table. The maximum half hour average of incoming shortwave radiation of 781 Wm^{-2} was measured 21.08.2018 at 01.30 pm, while the maximum half hour average of incoming longwave radiation of 361 Wm^{-2} was measured 22.08.2018 at 02.30 pm. Their mean values for the period were 145 Wm^{-2} and 313 Wm^{-2}, respectively. The minimum half hour average of incoming shortwave radiation was measured to < 0. This is most likely to be explained by noise that occurred in the measurements. The weather during the period was characterized by unstable and cloudy weather with changing cloud cover. There were only a few longer periods of some hours with a clear sky and sunny weather at daytime during the period of the study. The daily accumulated precipitation is shown in Table 4.2. There were two days with considerable amounts of rain. These rainfalls were caused by two small storms that hit Finse on 19.08.18 and 23.08.18. The highest wind gust was 22.30 ms^{-1}, while the mean wind speed for the whole period was 5.91 ms^{-1}, as shown in the left histogram in Figure 4.1. The right panel in Figure 4.1 shows the histogram of the wind direction. The predominant wind direction for the period was west-northwest.

Table 4.1: Numerical statistics of half hour meteorological variables measured at the Finse flux tower for the period 18.08.18-25.08.18.

Meteorological parameters	Min. value	Max. value	Mean	St. deviation
Net surface radiation (Wm^{-2})	-89.69	605.98	84.10	150.64
Shortwave incoming radiation (Wm^{-2})	-2.71	780.88	145.22	204.79
Longwave incoming radiation (Wm^{-2})	248.60	361.10	312.90	24.43
Air temperature (°C)	1.96	11.99	5.97	2.26
Relative humidity (%)	35.40	88.27	74.67	9.68
Wind direction (degree)	92.31	333.48	257.81	62.37
Wind speed (ms^{-1})	0.61	15.81	5.91	2.83

Table 4.2: Daily accumulated precipitation in mm at the Finse flux tower for the period 18.08.18-25.08.18.

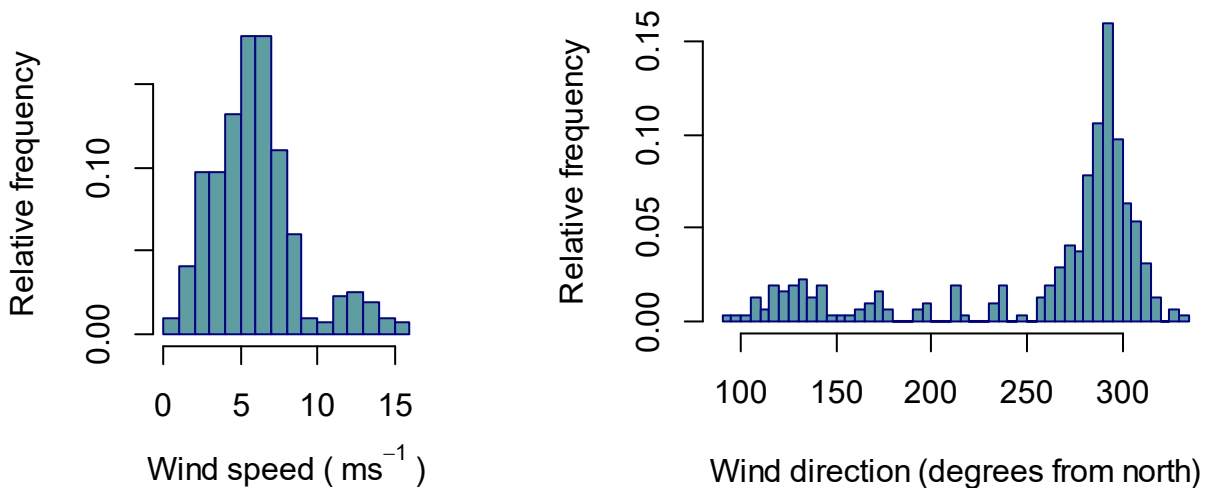| Date	Accumulated precipitation in mm
18.08.2018	2.80
19.08.2018	18.90
20.08.2018	0.60
21.08.2018	1.80
22.08.2018	0.20
23.08.2018	15.10
24.08.2018	0.90
25.08.2018	6.00

Figure 4.1: Histograms showing the wind speed (left panel) and wind direction (right panel) for the period 18.08.18-25.08.25, based on half hourly calculated mean values from the Finse flux tower. The y axes show the relative frequencies.

4.1.2   Sensitivity analysis

A visual inspection of the time series of shortwave incoming radiation, longwave incoming radiation, relative humidity and air temperature (Figure 4.2) revealed that there were to some extent dependencies among the variables. In the lower panel, a typical pattern was found with peaks of air temperature occurring at the same time as minimum values of relative humidity, and vice versa. This was quite coincident with the diurnal variation of the shortwave incoming radiation, as shown in the upper panel of Figure 4.2.

A correlation plot, including scatter and distribution plots, of net surface radiation, incoming shortwave and longwave radiation, air temperature, relative humidity, wind speed and wind direction, is shown in Figure 4.3. The strongest correlation (Pearson's correlation coefficient) of 0.9880 was found between R_{net} and the shortwave incoming radiation. This is also visualized by the strong linear dependence in the scatter plot panel. While both R_{net} and shortwave incoming radiation were positively correlated to the air temperature, they were, as expected, negatively correlated to the relative humidity. I.e. the increase/decrease in solar radiation was to some extent resulting in increased/decreased air temperature and decreased/increased relative humidity, as visualized in Figure 4.1. On the other hand, a positive correlation of 0.5180 was found between the longwave incoming radiation and relative humidity. This is reasonable, since an increase of especially low-level clouds and mist is closely related to the level of relative humidity. All three factors strongly impact the amount of incoming longwave radiation. The diurnal cycles probably explain much of the correlations found between the meteorological variables. The diagonal in the correlation plot shows the distribution of each of the radiative and meteorological variables investigated. As expected there was a peak in the distribution of observations for R_{net} close to zero, which is related to the absence of shortwave radiation during night, as shown by the blue line in Figure 4.2.
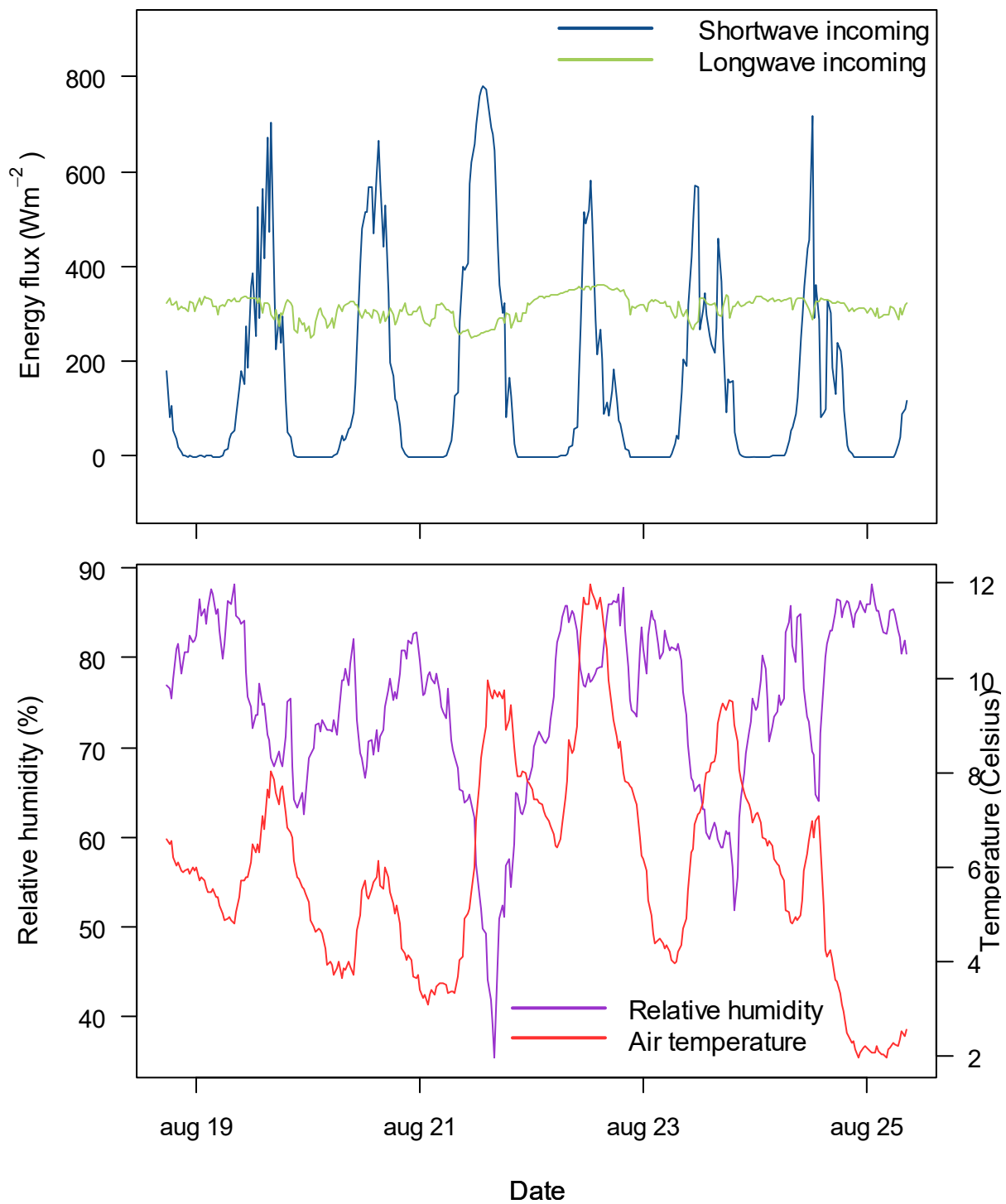
Figure 4.2: Time series of incoming shortwave and longwave radiation (upper panel) for the period 18.08.18 – 25.08.18. Lower panel shows time series for relative humidity and air temperature. An opposite pattern of peaks and minimum values is seen for the variables in the lower panel. This is to some extent dependent and coincident with the incoming shortwave radiation (blue curve) in the upper panel.
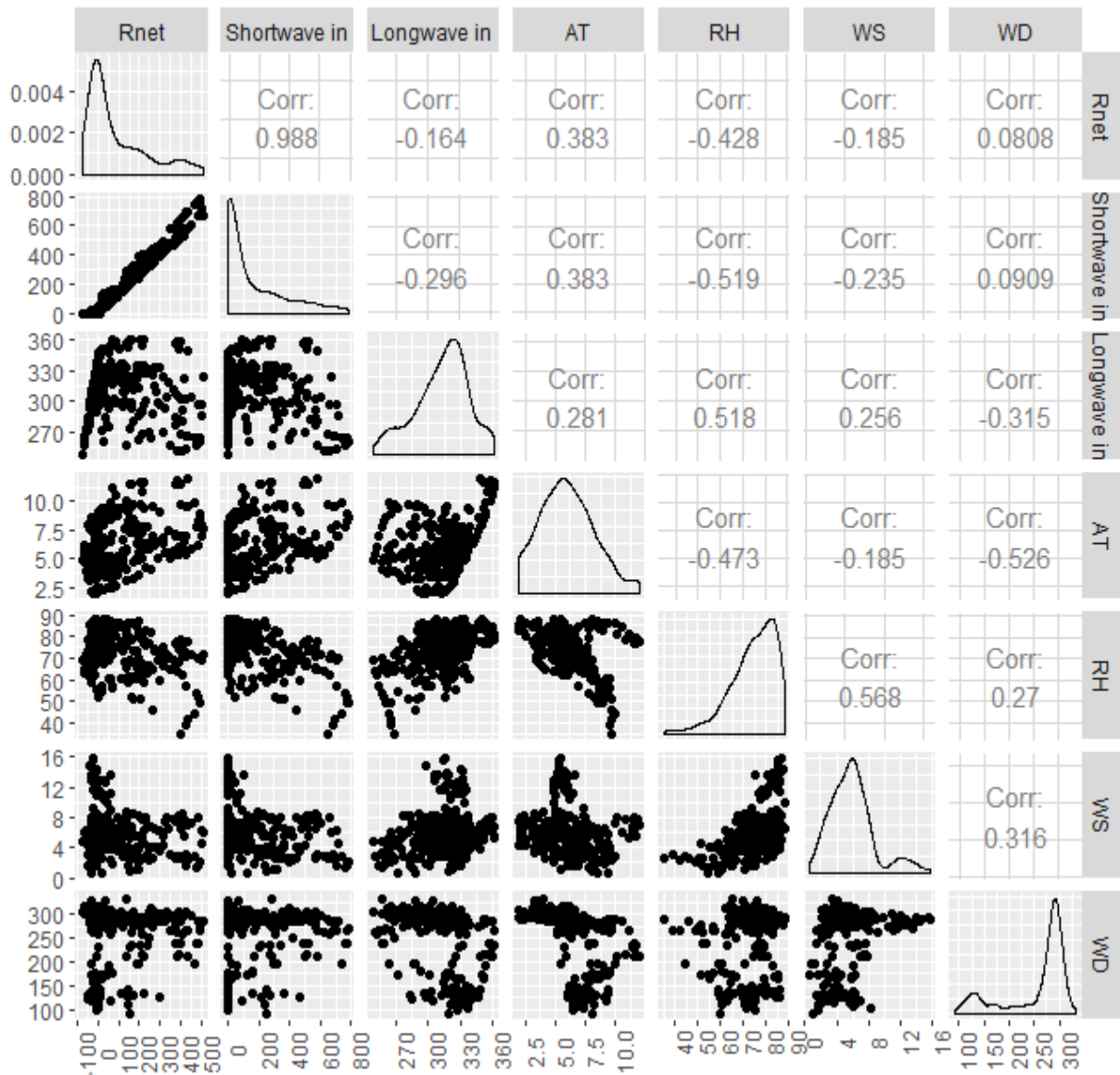
Figure 4.3: A correlation plot of the meteorological and radiative variables. The diagonal visualizes the distribution of the observations for each of the variables, while the part to the left of the diagonal shows the scatterplot between the variables. The part to the right of the diagonal gives the corresponding correlation coefficients (Pearson's correlation coefficient).

4.2   LM predictions of net surface radiation for different surface types

Visual inspection of normal Q-Q plots of the error distribution from the linear regression models fitted for the different surface types (Figure 4.4) revealed a moderate departure from normality. When emphasizing the central values of the plots of the error distribution, the normal distribution was a reasonably good approximation for all the different surface types. However, there was an overall tendency for all residual distributions to deviate from normality in the tails.

Especially for the surface types lichen-heathlands, water and late snow beds, heavier tails were found at the extremes. This indicated that the largest residuals were larger than expected, while the smallest residuals were smaller than expected. A subsequent analysis of the extreme errors revealed that the Cook's Distance errors were smaller than 0.35 for all models. This is thus an indication of no data observations with great influence for the performance of the linear regression models. For some surface types the biggest Cook's Distance was even smaller than 0.1. All models were also investigated by the studentized residual error. This error measurement revealed that all models except the regression model fitted for moderate snow beds, had a few studentized residuals greater than twice the standard deviation. This was thus an indication of some errors being statistically significant at 95 % level for the fitted regression models. The regression models for lichen-heathlands, mountain heathlands, water and extreme snow beds had all one big studentized residual of magnitude 3.19, -3.28, 3.06 and 3.18, respectively. These residuals should be considered as outliers.
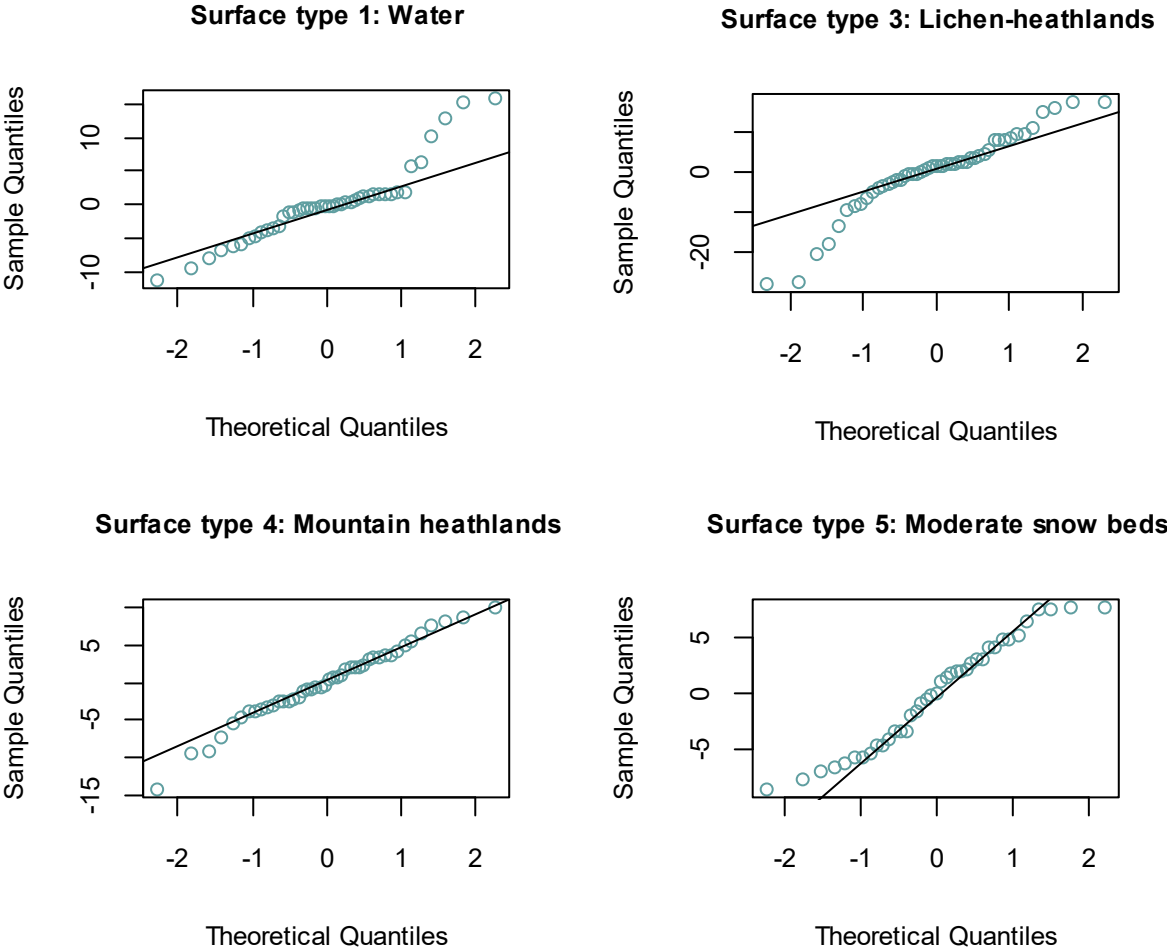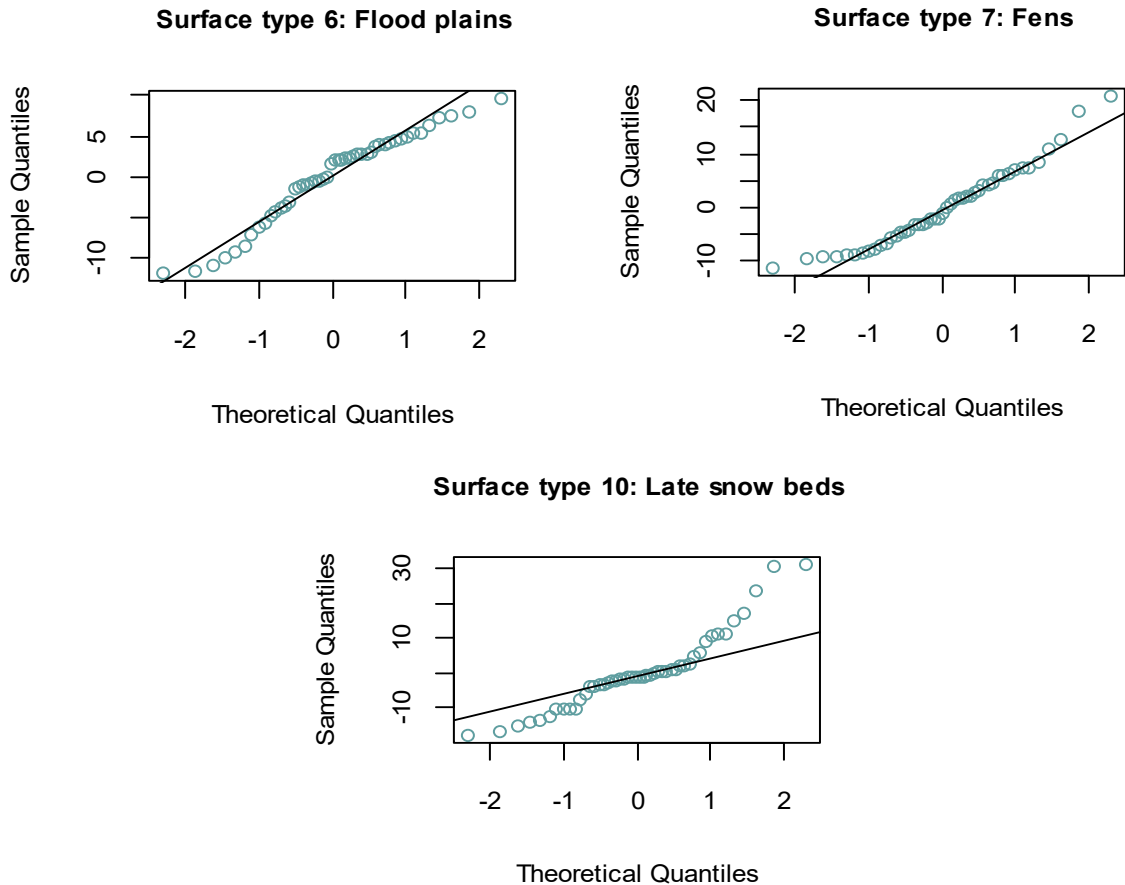

Figure 4.4: Cont.

Figure 4.4: Normal Q-Q plots of the residual distribution for the linear models fitted to each of the different surface types.

The prediction of net surface radiation by using linear regression was dependent on the local fitting of the regression coefficients, which implied that the surface cover affected the regression coefficients (Table 4.3). The α's, which represent the intercept with the y axis, varied from -466 Wm^{-2} (lichen-heathlands) to -233 Wm^{-2} (late snow beds). A difference of more than 230 Wm^{-2} between the lowest and highest α's was thus found between the surface types. The β_1's, which may be interpreted as the mean change of net surface radiation when the incoming shortwave radiation increases/decreases with one Wm^{-2} at the same time as the longwave radiation is kept constant, varied from 0.71 to 0.78 for all the vegetation surface types. For water, the β_1 was estimated to 0.93. The highest β_2, of 1.38, was found for lichen-heathlands, while the second highest, 1.02, was found for water. The β_2's may be interpreted as the mean increase/decrease of net surface radiation for the different surface types when the longwave incoming radiation increases/decreases with one Wm^{-2} and the shortwave incoming radiation remains unchanged.

Table 4.3: Regression coefficients for the individual fitted linear regression models used for predicting net surface radiation for the different surface types.

| Surface type	Regression coefficients		
	α	β_1	β_2
1: Water	-365.16	0.93	1.02
3: Lichen-heathlands	-466.55	0.74	1.38
4: Mountain heathlands	-286.99	0.72	0.84
5: Moderate snow beds	-223.96	0.77	0.65
6: Flood plains	-312.14	0.75	0.93
7: Fens	-314.03	0.78	0.91
10: Late snow beds	-224.13	0.71	0.66

Table 4.4: Statistical results for both the linear regression models and artificial neural networks used for predicting net surface radiation for the different surface types. The R^2 and RMSE is an evaluation of the training process/fitting to the data, while the RMSEP and R^2_{pred} evaluate the predictive power and accuracy of the models based on a LOOCV.

| Surface type	Number of measurements	Model	R^2	RMSE	RMSEP	R^2_{pred}
1: Water	44	ANN	0.9982	0.70	8.64	0.9978
		LM	0.9988	5.77	5.85	0.9987
3: Lichen-heathlands	49	ANN	0.9979	0.43	10.31	0.9946
		LM	0.9952	10.02	10.51	0.9943
4: Mountain heathlands	44	ANN	0.9983	0.10	7.46	0.9973
		LM	0.9985	5.13	5.51	0.9981
5: Moderate snow beds	39	ANN	0.9957	0.24	5.14	0.9973
		LM	0.9971	4.98	5.18	0.9966
6: Flood plains	48	ANN	0.9988	0.58	8.40	0.9981
		LM	0.9990	5.59	5.69	0.9989
7: Fens	47	ANN	0.9972	0.28	10.52	0.9957
		LM	0.9971	7.51	7.76	0.9966
10: Late snow beds	48	ANN	0.9988	0.15	10.30	0.9977
		LM	0.9967	11.07	11.54	0.9962

According to the statistical results given in Table 4.4, the LMs showed a high quality for the fitted models for all surface types, by explaining more than 99% of the variation in net surface radiation by the models. The small decrease from the R^2 to R^2_{pred} revealed that the fitted LMs predicted net surface radiation well for new independent observations. The LMs' RMSE was between 4.98 – 11.07 Wm^{-2}, while the RMSEP was found to be in the range of 5.18 – 11.54 Wm^{-2}. For all surface types there was only a small increase from the RMSE to the RMSEP. The biggest difference was found to be 0.49 Wm^{-2} (lichen-heathlands), but for the other surface types the difference between RMSE and RMSEP was considerably smaller. This indicated that the linear models were well fitted to both the training data and the independent observations of incoming shortwave and longwave radiation.

Predictions of continuous time series of net surface radiation (for both the LMs and the ANNs) for the whole period are shown in Figure 4.5. Each surface type is plotted in a separate panel. The diurnal variation in net surface radiation was predicted well for all surface types, with evident peaks during midday due to the dominating incoming shortwave radiation at daytime. At night time a typical pattern of small negative values of net surface radiation was found. This is reasonable due to the absence of incoming shortwave radiation, which means that long wave radiation is the only controlling mechanism for the radiative balance. The visualization revealed that the predictions for all surface types managed to capture the sudden change in incoming shortwave radiation caused by change in cloud cover very well. This is shown as the rapid shift in spikes for most days during daytime. For all surface types the predictions of the LM's were in good agreement compared to the actual measurements (illustrated as the blue circles in Figure 4.5).

Surface type 1: Water
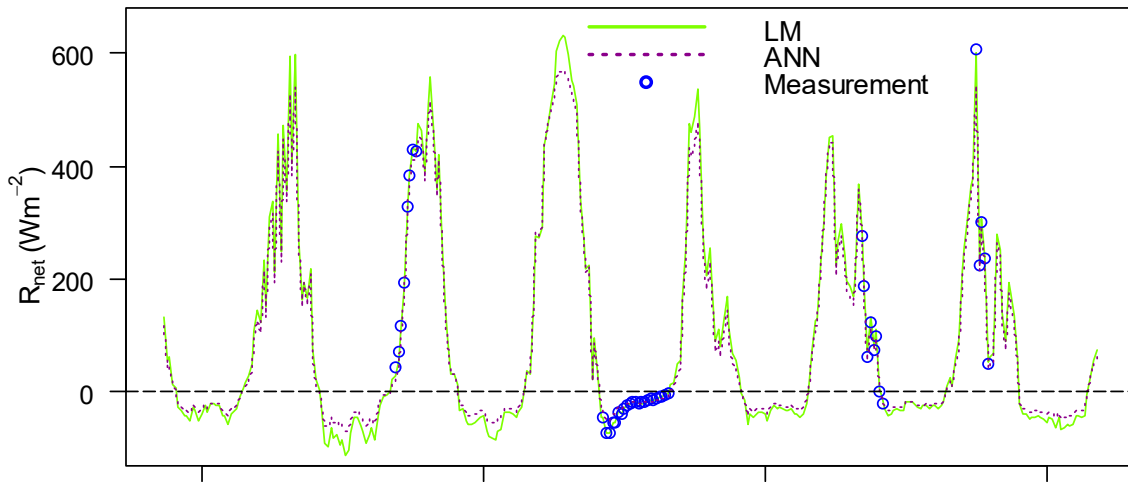
Surface type 3: Lichen-heathlands
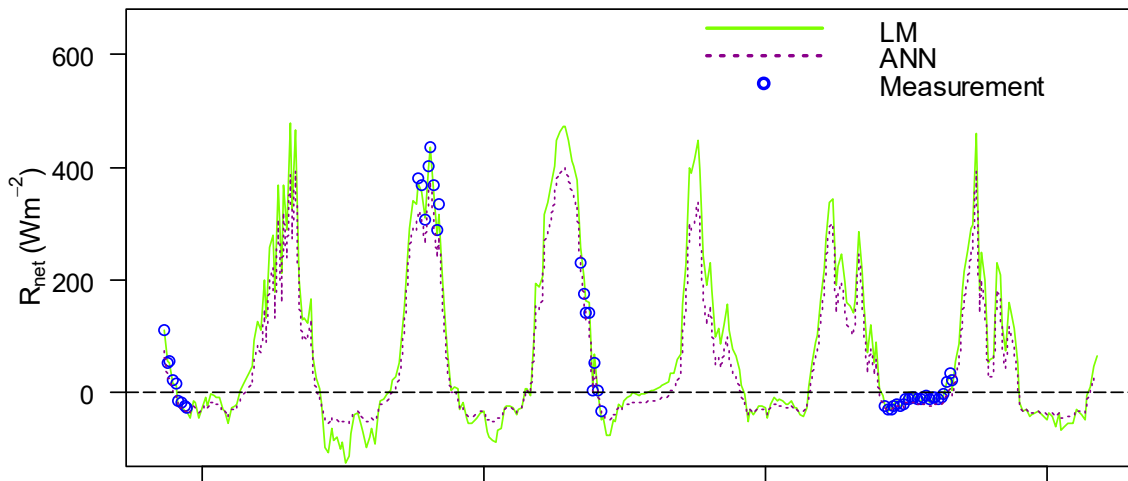
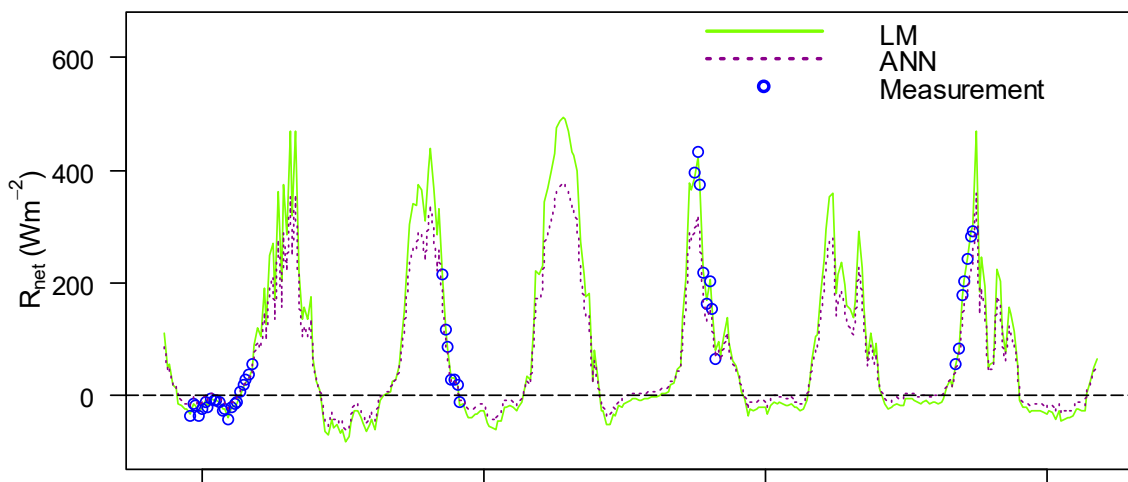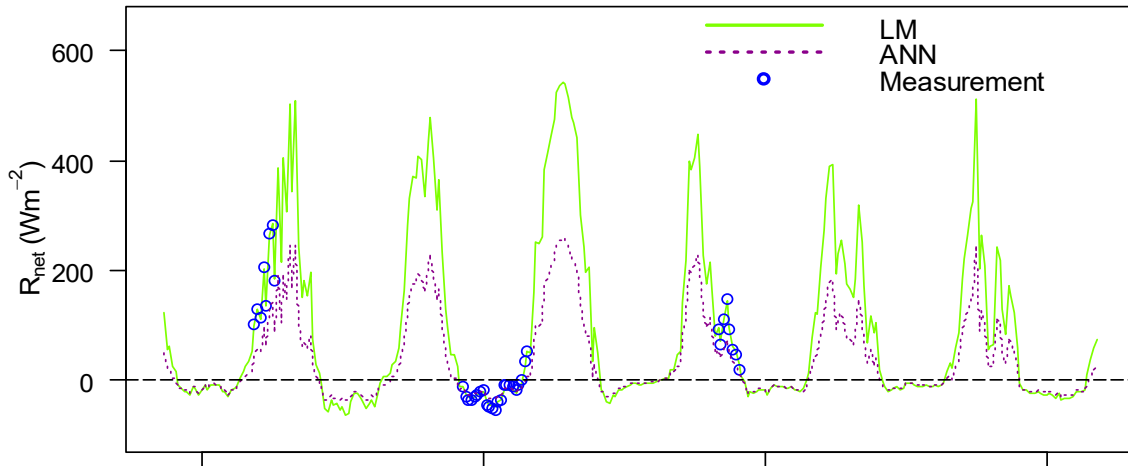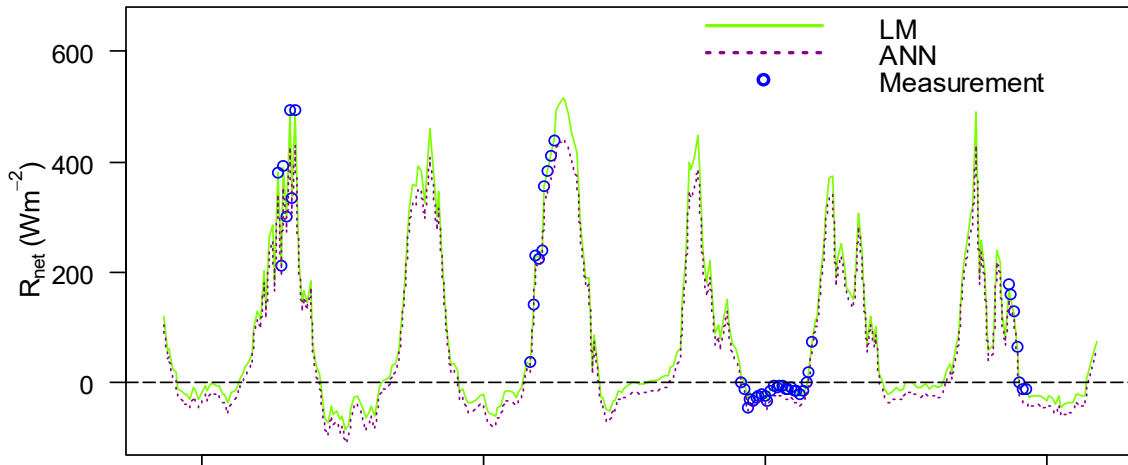
Surface type 4: Mountain heathlands

Figure 4.5: Cont.

Surface type 5: Moderate snow beds

Surface type 6: Flood plains

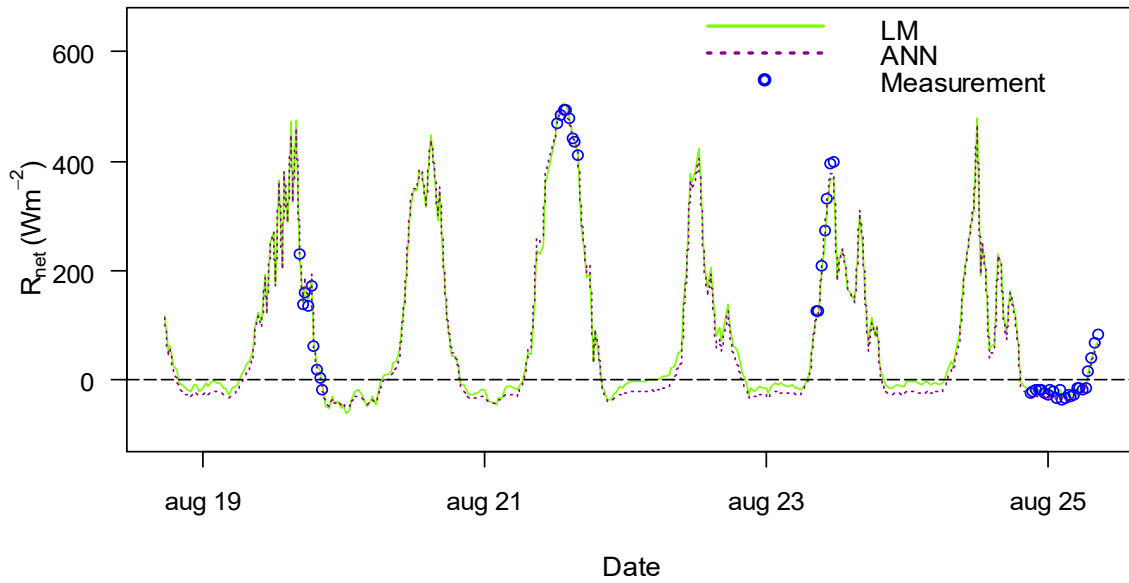# Surface type 7: Fens
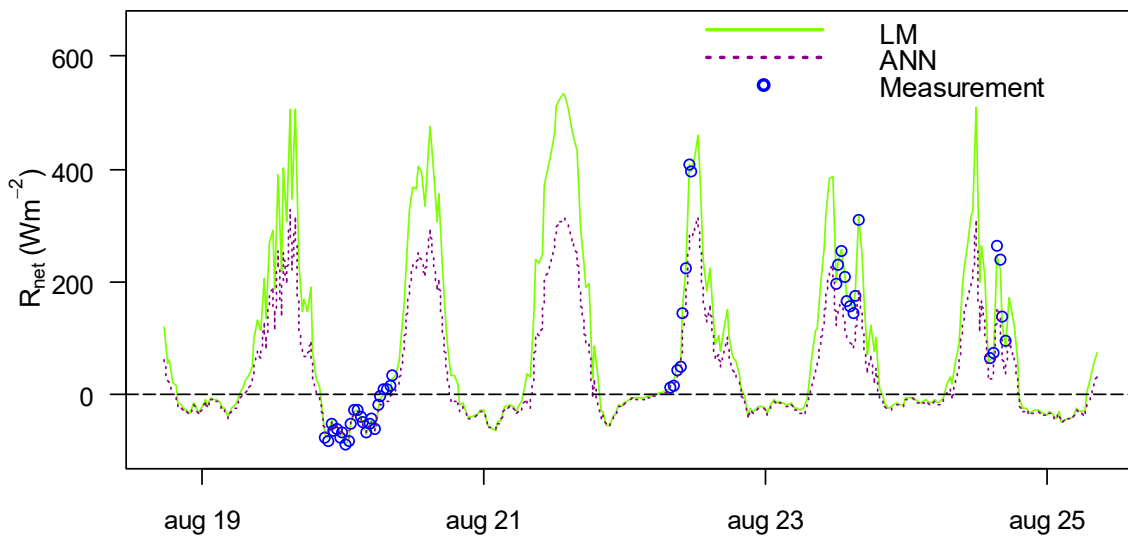
Figure 4.5: Cont.

Figure 4.5: Predicted time series of net surface radiation for the different surface types (different panels) for the period 18.08.18 – 25.08.18. The solid-drawn, green lines are for the LMs, while the dotted, purple lines show the predictions of the ANNs. The blue circles visualize the actual measurements of R_{net} for each of the different surface types, which were used to train the models.

4.3   ANN predictions of net surface radiation for different surface types

According to the statistical results given in Table 4.4, the ANN showed a high quality for the fitted models for all surface types by explaining more than 99% of the variation in net surface radiation by the models. No distinct pattern regarding coefficients of determination for ANNs versus LMs was found. Coefficients of determination displayed greater variation among the different surface types. Nevertheless, a clear tendency of a larger decrease from the R^2 to R^2_{pred} was found for the ANNs than for the LMs. This may be interpreted as the LMs were predicting the net surface radiation evenly well, regardless of whether the observations of incoming shortwave and longwave radiation were independent of the training data or not. The quality of the ANNs and their predictive power were more dependent of the change from training data to new independent input observations. For the ANN fitted for moderate snow beds, the correlation coefficient was 0.9957, while R^2_{pred} was calculated to 0.9973.

The ANNs' RMSE were in the range between 0.10 – 0.70 Wm^{-2}. When comparing RMSE for the LMs and the ANNs for all the surface types, a much higher RMSE was found

for the LMs. However, the difference between the RMSE and RMSEP, was found to be greater than a factor of 10 for all ANNs, and for some of the surface types the ANN's difference between RMSE and RMSEP increased with a factor of 74. For all surface types except lichen-heathlands, the RMSEP of the ANNs exceeded the RMSEP of the LMs. The findings of the abnormal large increase of RMSE to RMSEP of the ANNs, revealed an overfitting of the ANNs.

Overall, the time series revealed a fairly good pattern of accordance between the ANN predicted and LM predicted net surface radiation. However, a main feature from the visualization was that for almost all surface types the LMs predicted the extreme values and peaks of net surface radiation during daytime better than the ANN. Especially for surface type 5, moderate snow beds, and surface type 7, fens, the difference in daytime predictions between the LM and ANN were considerable, with the largest differences of 285 Wm^{-2} and 221 Wm^{-2}, respectively. This was found at 13.30 pm on 21.08.18. For surface type 10, late snow beds, an almost perfect match between the LM and ANN predicted R_{net} occurred for the whole time series. The comparison of the predicted times series provided by the ANNs and actual measurements (illustrated as the blue circles in Figure 4.5), revealed that there was an inconsistence between the predictions and measurements. This was mainly pronounced during daytime, especially found for the peaks and extremes during midday and for the sudden changes due to clouds.

4.4   Comparison of net surface radiation for different surface types

The ANCOVA revealed that there were statistically significant differences in LM predicted net surface radiation among all surface types except for three of them. The exceptions of difference were found between late snow beds and flood plains, between late snow beds and moderate snow beds, and between flood plains and fens. It was thus a statistically significant difference in albedo and heat balances for almost all surface types. The smallest p-values from the ANCOVA were found between water and the other surface types, where all of them were $< 2.2*10^{-16}$. The strong distinction of water was also revealed from the visualization of the time series of the seven surface types (Figure 4.6). Here it was found that water had considerably higher net surface radiation during daytime than the other surfaces. At the same time, the visualization showed that during daytime, especially with clear sky without clouds, net surface radiation was found to be systematically lowest for lichen-heathlands. These findings seem

reasonable due to the low albedo of water, ~0.05 - 0.10, and the much lighter surface provided by lichens. For the remaining surface types, the plotted time series revealed that during daytime, net surface radiation was found to be highest for moderate snow beds, followed by fens, flood plains, late snow beds and mountain heathlands.

Another interesting observation found during nighttime, were that both water and lichen-heathlands excelled with systematically lower net surface radiation than the other surface types. The net surface radiation at night is mainly controlled by the longwave components. Such a clear distinction between water and lichen-heathlands on one hand and the other surface types on the other, was thus explained by (i) higher emissivity, (ii) higher temperatures and/or (iii) considerable difference of the mechanisms controlling the heat balances. These mechanisms are photosynthesis, evapotranspiration, ability to capture and store precipitation and the access of water. According to Brewster (1992) the thermal emissivity (for surface temperatures of 300 K) is 0.92 – 0.96 for vegetation, ~0.96 for water and 0.88 – 0.92 for rocks. The high emissivity of water may therefore to some degree explain the large outgoing longwave radiation found during night. However, since lichens are spectrally similar to other vegetation for thermal infrared wavelengths (Abbot et al., 2013), the low net surface radiation for lichen-heathlands was mainly explained by the higher temperature during night compared to the other vegetation surfaces. The difference of 30 Wm^{-2} in net surface radiation between mountain heathlands and lichen-heathlands found 21.08.18, at 2 am was therefore mainly explained by temperature differences. However, for surface type 5, which consists of boulder fields and moderate snow beds, a potential lower emissivity of the rocks (according to Brewster, 1992) may play a noticeable role for emissions of longwave outgoing radiation.
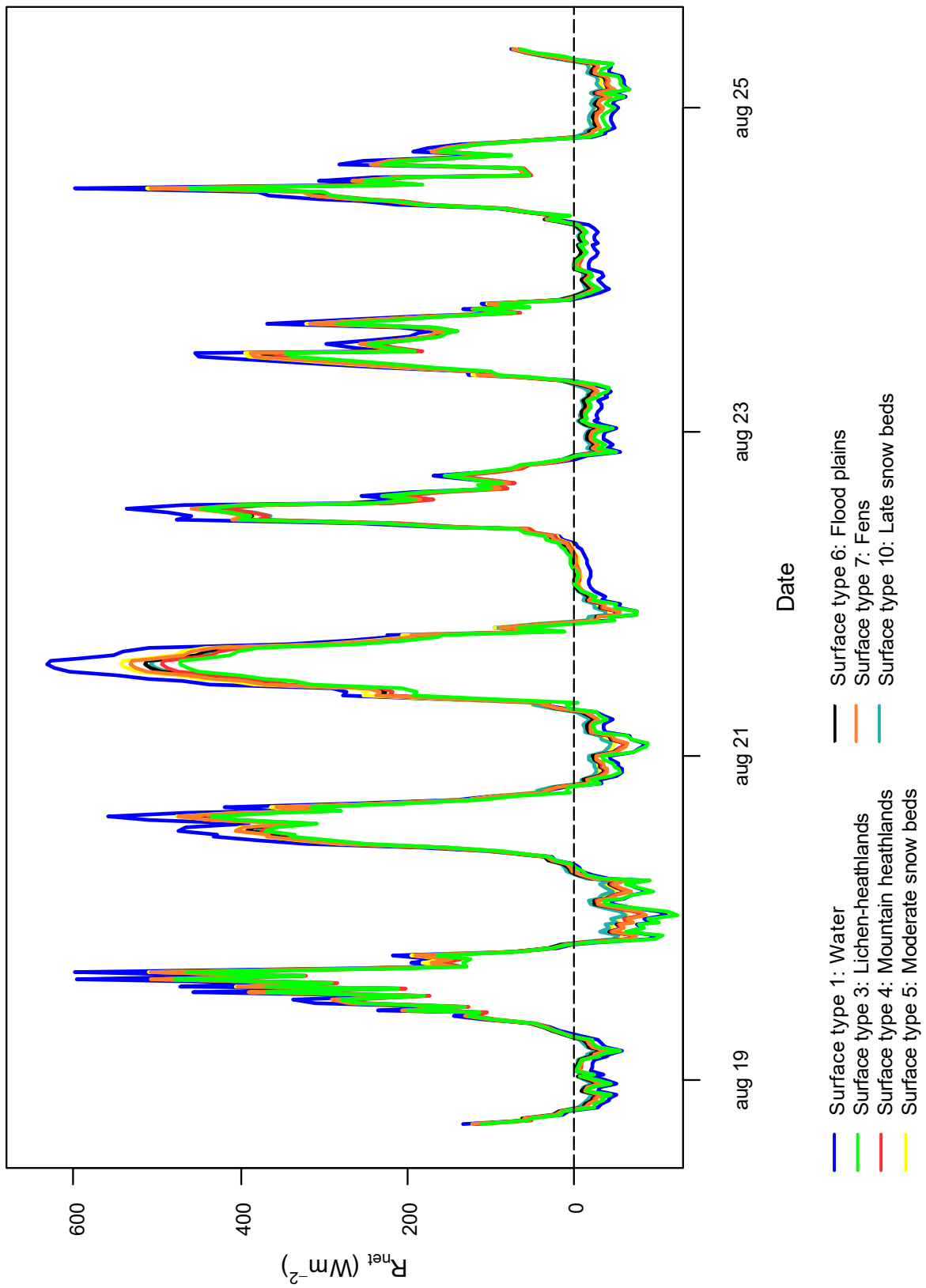
Figure 4.6: Comparison of net surface radiation predicted by LMs for the different surface types.

51

4.5   Footprint analysis

The estimated footprint climatology, i.e. the aggregated footprints estimated for all half hourly measurements of the time series of the turbulent fluxes, is shown in the surface type map in Figure 4.7. The shaded area covers 80% of the area where the turbulent energy has exchanged between the surface cover and overlying atmosphere for the investigated period between 18.08.18 and 25.08.18. The footprint climatology revealed that approximately two thirds of the contribution of the turbulent energy fluxes came from the surface lying northwest of the tower, while the last one third came from the southeastern area. Thus, ~28% of the contribution to the measurements came from open water (Table 4.5). The river running southeast of the tower was a predominant source. Among the vegetation surface types, it was found that fens, mountain heathlands and lichen-heathlands contributed the most to the turbulent energy exchange for the period. 93.91% of the total footprint area was covered by the seven surface types investigated in the study, while 6.09% was covered by nature types not investigated in this study. One half of these contributions came from surface type 0, anthropogenic nature types, while the last half originated from surface type 2. As shown, and expected, there was a high agreement between the predominant wind direction for the period (Figure 4.1, right panel) and the main source area contributing to the flux tower's footprint.

Table 4.5: The percentage contribution of each surface type to the 80% footprint climatology of the turbulent energy fluxes.

Surface type	Percentage contribution, p_i, to the turbulent fluxes' footprint (%)
1: Water	27.95
3: Lichen-heathlands	12.02
4: Mountain heathlands	13.05
5: Moderate snow beds	10.56
6: Flood plains	6.29
7: Fens	17.21
10: Late snow beds	6.83

Surface types

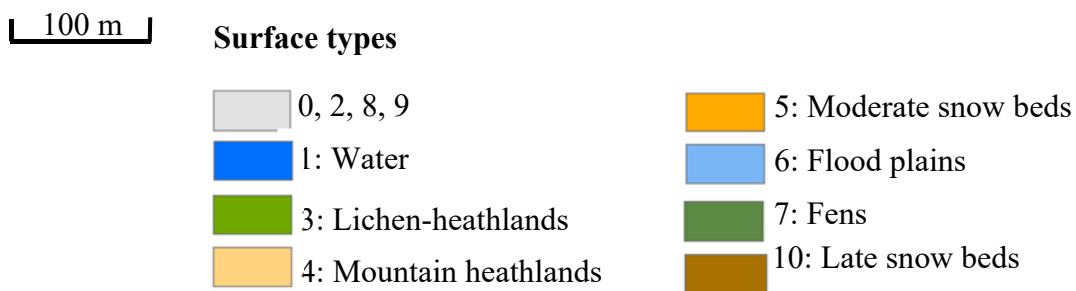|			
⬜	0, 2, 8, 9	🟧	5: Moderate snow beds
🟦	1: Water	🟦	6: Flood plains
🟩	3: Lichen-heathlands	🟩	7: Fens
🟨	4: Mountain heathlands	🟫	10: Late snow beds
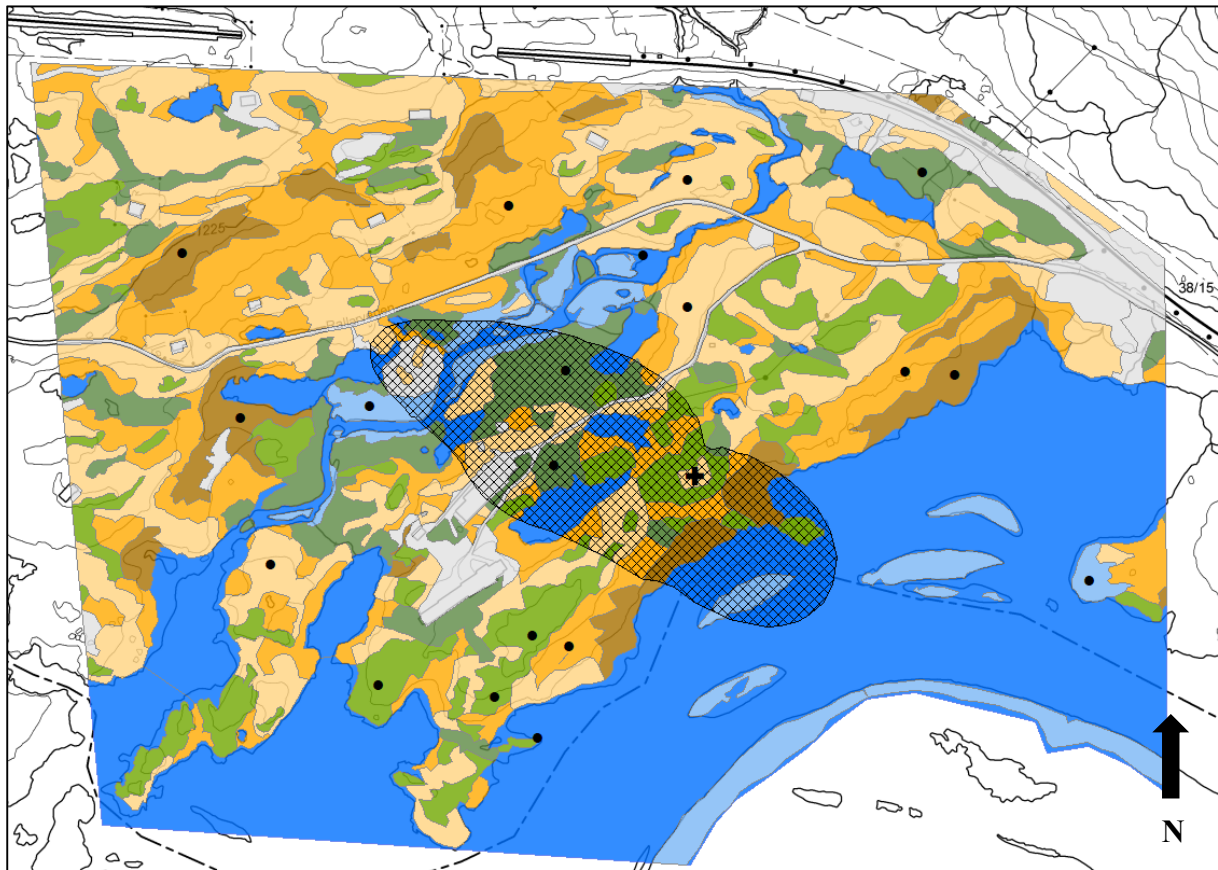
Figure 4.7: As Figure 3.6. The shaded area visualizes the 80% footprint climatology area during the 18.08.18 – 25.08.18 period, estimated by the method of Kljun et al. (2015) for the turbulent fluxes by using the online service data processing provided by Kljun et al.

The comparison of net surface radiation measured by the Finse stationary flux tower and the LM predicted net surface radiation where the heterogeneity of the surface cover was accounted for by weighting with the contribution from different surface types, $\tilde{R}_{net}$, are given in Figure 4.8. The percentage contribution of each surface type which was used to compute the weighted net surface radiation, is shown in Table 4.5. Inspection of Figure 4.8 showed that there was a high degree of consistency between the LM predicted $\tilde{R}_{net}$ and the net surface radiation

measured by the tower. Generally, the most pronounced difference was found during night, where the LM predicted $\tilde{R}_{net}$ had greater negative values than the R_{net} measured by the stationary flux tower. This was an indication that the LM predicted $\tilde{R}_{net}$ had higher values of outgoing longwave radiation than R_{net}. There were also tendencies of higher extreme values (peaks) at daytime for R_{net} measured by the stationary flux tower, than for the LM predicted $\tilde{R}_{net}$, but these findings were not consistent throughout the whole period.
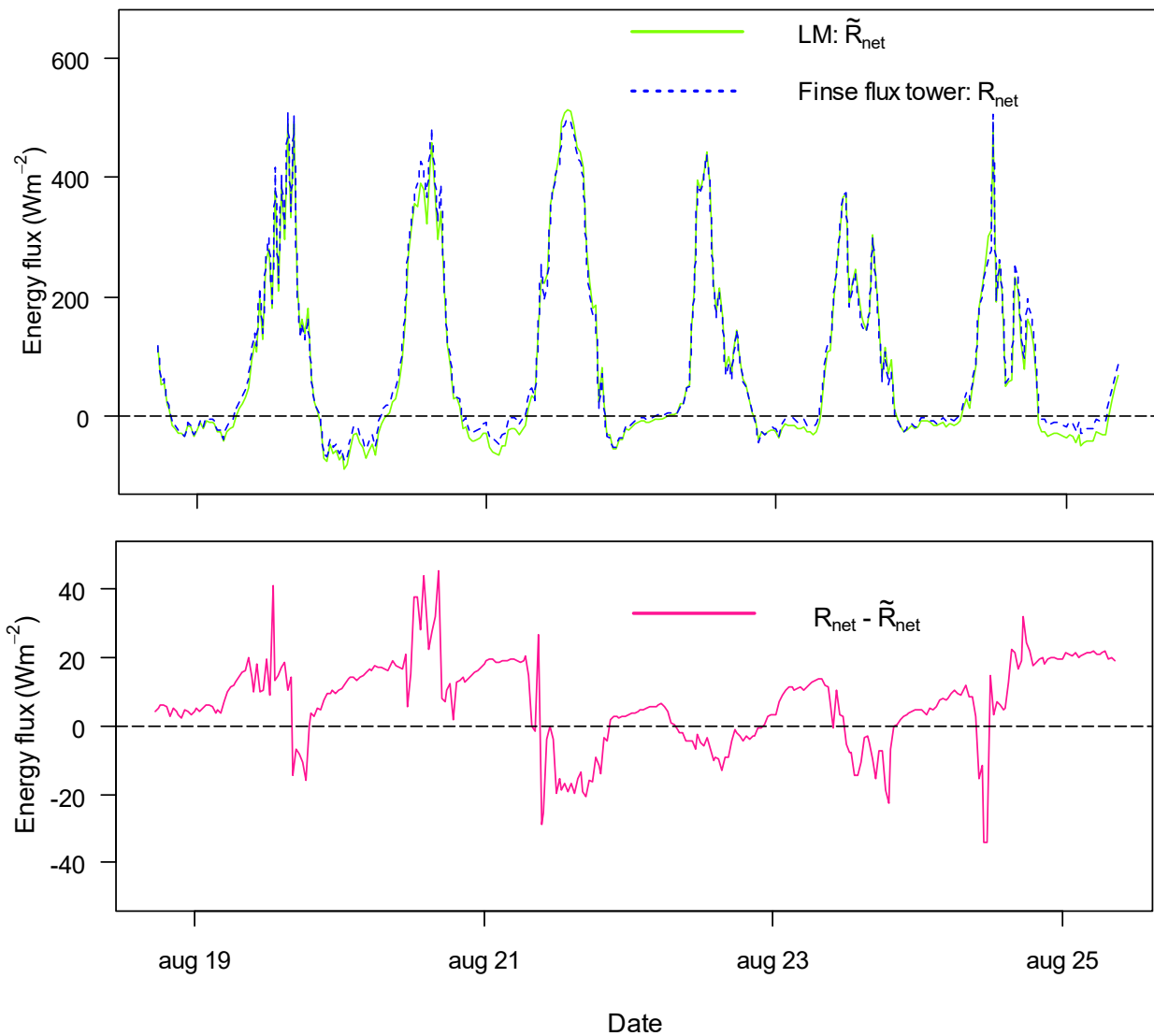
Figure 4.8: Upper panel: The solid, green line represents net surface radiation where the surface heterogeneity is accounted for by weighting the LM predictions of the different surface types by their percentage contribution of the turbulent flux tower footprint. The dashed, blue line represents R_{net} measured by the stationary flux tower at Finse. Lower panel: The pink line represents the difference between net surface radiation measured by the Finse flux tower and the LM predicted footprint weighted net surface radiation.

4.6   Energy balance closure

42% of the half hour data were discarded due to low quality of the estimates of the turbulent fluxes of sensible and latent heat. Figure 4.9 shows the half hourly averaged fluxes throughout the day for the period 18.08.18 – 25.08.18. The sensible heat flux was found to transport heat away from the surface in daytime from 9 am to 10 pm, while at night there was a transport of heat from the atmosphere towards the surface due to lower temperature of the surface than for the overlying air. The latent heat flux revealed a transportation of energy as vaporization heat from the surface towards the atmosphere throughout the whole day. As expected, the soil heat flux played a minor role of the energy exchange, with positive values between 12 am to 10 pm, thus indicating an energy transport into the soil. A time lag of approximately two to three hours was found between the net surface radiation and the soil heat flux.
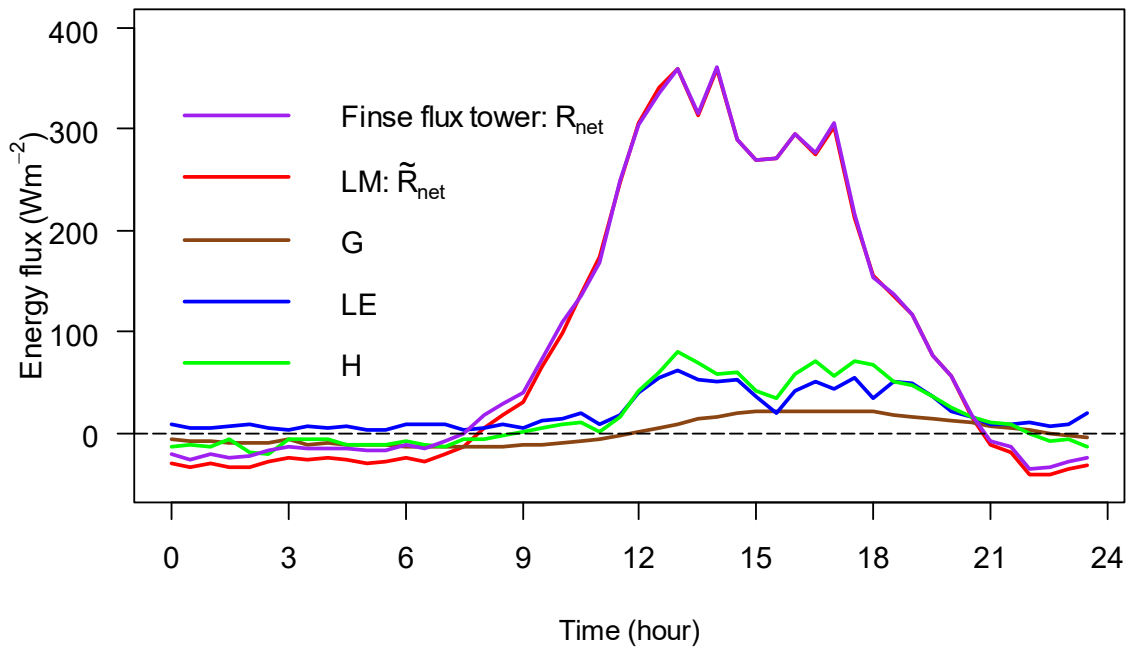
Figure 4.9: Half hourly averaged fluxes, for the period 18.08.18 – 25.08.18, showing the diurnal variations of the latent heat (LE), the sensible heat (H), the soil heat flux (G), the net surface radiation (R_{net}) measured by the Finse flux tower, and the LM predicted net surface radiation ($\tilde{R}_{net}$) accounting for the heterogeneity of the surface cover.

The relationships between the LM predicted $\tilde{R}_{net}$ and the flux measurements of respectively sensible heat (H), latent heat (LE) and soil heat flux (G) were

$$H = 3.62 + 0.23 * \tilde{R}_{net} \tag{4.1}$$

$$LE = 19.20 + 0.13 * \tilde{R}_{net} \tag{4.2}$$

$$G = -4.58 + 0.05 * \tilde{R}_{net} \tag{4.3}$$

According to these results, the sensible heat flux and the latent heat flux accounted for 23% and 13% of the LM predicted $\tilde{R}_{net}$, respectively. The soil heat flux accounted for only 5% of the LM predicted $\tilde{R}_{net}$.

The energy balance closure (Figure 4.10) was calculated to 37% when assessing the energy balance with the ordinary least squares regression and by using the net surface radiation measured by the Finse flux tower. A similar closure of 37% was calculated for the same technique, but where LM predicted $\tilde{R}_{net}$ was used as available energy instead of R_{net}. However, the coefficient of determination for the two energy closures were found to be 0.5789 and 0.5913, respectively. Thus, a small increase of 1.24 percent points was found between the two regressions. This indicated that the variation of the turbulent fluxes of sensible and latent heat was explained slightly better by the LM predicted $\tilde{R}_{net}$ than by the R_{net} measured by the Finse flux tower.

The calculations of the energy balance ratio revealed that the turbulent fluxes accounted for 53.80% of the incoming available energy measured by Finse flux tower. When the footprint corrected net surface radiation based on the predictions of the LMs was used as available energy together with the soil heat flux, the EBR was found to be 58.20%. An increase of 4.40 percent points was thus found for the energy balance closure when the heterogeneity of the surface cover was accounted for. From the visual inspection of half hourly averaged fluxes (Figure 4.9), it was reasonable to believe that a major cause of the increase of the EBR was a lower net surface radiation at night from the heterogenous surface than measured by the Finse flux tower. Thus, the higher emissions of long wave radiation from the heterogenous surface cover at night led to a decrease of the available energy for the period. The imbalance between the incoming and outgoing energy was therefore decreased.

Energy balance closure based on R_{net} from Finse flux tower

(upper panel)

Legend:
y = 19.49 + 0.37 * x
$R^2 = 0.5789$
EBR = 0.5380

H + LE (Wm^{-2})

R_{net} - G (Wm^{-2})

Energy balance closure based on LM predicted $\widetilde{R}_{net}$

(lower panel)

Legend:
y = 22.41 + 0.37 * x
$R^2 = 0.5913$
EBR = 0.5820

H + LE (Wm^{-2})

$\widetilde{R}_{net}$ - G (Wm^{-2})
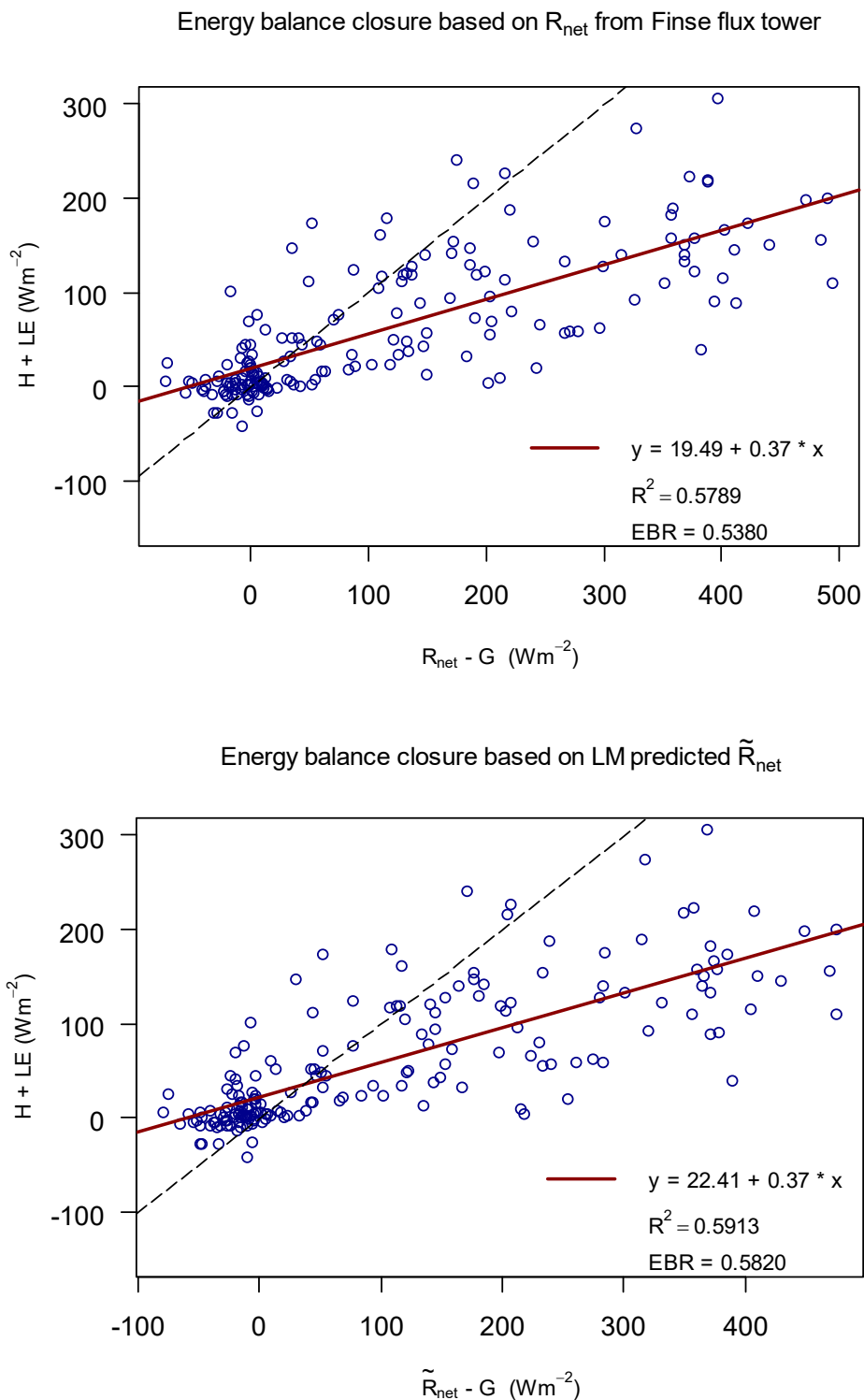
Figure 4.10: A comparison of the energy balance closure investigated with net surface radiation measured by the Finse flux tower (upper panel) and the energy balance closure investigated with the LM predicted net surface radiation corrected for the heterogeneity of the surface cover (lower panel). Both energy closures were investigated for the period 18.08.18 – 25.08.18. The red lines illustrate the regression lines obtained by OLS regression between the available energy (x axis) and the turbulent energy (y axis). The dashed black lines visualize the perfect energy balance closure of 100 % with an intercept of zero and a slope equal to 1. The energy balance ratio (EBR) is represented in the legends in both panels.

5 Discussion

5.1 Suitability of ANN and LM as predictive models for net surface radiation

The statistical evaluation of the LMs showed a high quality for the fitted models for all the different surface types, with correlation coefficients for the prediction in the range of 0.9943 – 0.9989 (Table 4.4). The RMSEP for the LMs was found to be in the range between 5.18 – 11.54 Wm^{-2}. For the surface types lichen-heathlands, moderate snow beds and late snow beds, both RMSEP and R^2_{pred} was higher for the ANNs than for the LMs. However, by inspection of the visual times series of lichen-heathlands and moderate snow beds (Figure 4.5), a better match was found between the measurements and the predictions for the LMs, than between the measurements and the ANN's predictions. This disagreement is explained by the failure of the ANNs to predict net surface radiation well for extreme values and peaks during daytime. The LMs predicted net surface radiation very well for all surface types throughout both day and night, with an almost perfect match between the measurements and predictions. Thus, it was a general tendency that the ANNs were unable to predict the extreme values and peaks in net surface radiation at midday for most surface types as well as the LMs.

When evaluating a model used for predicting net surface radiation, a decisive characteristic for the model is to be able to capture the extreme values when having clear sky during day and rapid shifts of shortwave incoming radiation caused by clouds. A model that fails to account for the huge variation of shortwave incoming radiation and which is not capable of predicting the extremes of net surface radiation, is thus not suitable for the purpose. Especially when investigating the different surface types' ability to reflect the incoming shortwave radiation, an accurate prediction of net surface radiation at midday is essential. Otherwise, incorrect and biased evaluations of the albedo characteristic may be the result.

From the comparison of the RMSE and RMSEP (Table 4.4) for the ANNs, a clear indication of overfitting was found. Artificial neural networks are quite complicated models, and overfitting is not uncommon. Their ability to learn non-linear relationship and make advanced memorizations of the training data is advantageous when having complex data sets and may therefore be an important complement to statistical models. Mahalakshmi et al. (2016a) and Geraldo-Ferreira et al. (2011a) reported a successful estimation of net surface radiation based on meteorological variables, for both LMs and ANNs. However, in these studies data were collected for respectively 11 months and four months, thus providing a much greater

data basis when training models for generalized purpose. In this study, it is believed that an overfitting is mainly explained by the small datasets with too few observations available for the training process. Therefore, the ANNs were too complex even though it was a strong relationship between output and input variables and even though all ANNs, except for the neural network fitted for lichen-heathlands, had only one single hidden layer with few hidden neurons.

5.2 Importance of different surface types for net surface radiation

The ANCOVA revealed that there was a statistically significant difference in net surface radiation between the different surface types. Only between moderate snow beds and late snow beds, between late snow beds and flood plains, and between flood plains and fens, no statistical difference was found. It was not always possible to detect a clear difference between the surface characteristic of the moderate snow beds and the extreme snow beds when the surfaces were investigated in field. It is therefore reasonable that a minor difference was found between those two. The moderate snow beds were also the surface type which consisted of most different nature types. This was reflected in the large variation of the surface cover between the different measurement sites within this surface type.

The higher temperatures of the lichen-heathlands and water during nighttime give a clear distinction between these surfaces and the others. Due to water's high heat capacity, a damped diurnal variation in surface temperature is likely to occur, compared to vegetation. It is therefore reasonable that water has more negative net surface radiation than the other surfaces during night. The high emissions of longwave radiation during night for lichen-heathlands is likely to be related to the lichens' large water storage capacity. Their sponge-like behavior leads to a maximum saturation after just some minutes when exposed to water. The saturation happens when exposed to rain, fog, dew or only high air humidity. Since the weather during the study period was quite humid and rainy, the lichen-heathlands remained quite wet during both days and nights. The lichen-heathlands were therefore storing considerably amounts of water despite their relative shallow height above the solid rock. The high emissions of longwave radiation from the lichen-heathlands during night is therefore likely to happen because of the damped diurnal variation of temperature in the surface cover. If the lichen-heathlands had been dehydrated during the period, the emissions of longwave radiation would have been lower during night (Kershaw, 2010).

The differences in net surface radiation obtained between the different surface types at midday, were mainly caused by significant differences in the reflecting properties of the shortwave incoming radiation of the surfaces. The longest period of sunny and clear sky weather, which provided considerable amount of direct incoming shortwave radiation, was during midday, ~12.30 pm – 14.30 pm, 21.08.18. The largest differences in net surface radiation obtained throughout the whole study period occurred for some of the different surface types during these hours. Worth noticing was the difference between fens and lichen-heathlands of 62 Wm^{-2}, the difference between mountain heathlands and fens of 39 Wm^{-2}, and the difference between moderate snow beds and mountain heathlands of 50 Wm^{-2}. This can be understood as a significant difference of albedo between the surface types. An even more pronounced distinction in net surface radiation due to the albedo effect is expected to be detected when longer periods with stable direct incoming shortwave radiation occurs.

It must be expected that shadows and disturbances of the radiation tower and logger-box influenced the measurements performed in field. However, these influences are assumed to not differ substantially between the different measurement sites and the different surface types. Due to uncertainty in the vegetation map and uncertainty in the precision of the GPS used to navigate to the measurement points, it must be expected that for some measurements smaller contribution from other surface types may have occurred.

5.3   Assessment of the energy balance closure

As one of the main goals, this study intended to investigate how the effect of non-corresponding source areas between the turbulent fluxes and net surface radiation contributed to the energy imbalance between the turbulent fluxes and the available energy at Finse. The Finse flux tower is placed in a highly heterogenous environment, both in terms of surface cover and topography. A thorough understanding of how net surface radiation differs for different surface types is thus important when analyzing potential causes for the inconsistence between incoming and outgoing energy.

Based on the energy balance closure investigated by OLS regression, no improvement was found between the available energy and turbulent fluxes when correcting for the heterogeneity of the surface cover. Both closures were calculated to 37%. However, the coefficient of determination increased by 1.24 percent points. In this study, the footprint climatology was used to weight the different surface types to find $\tilde{R}_{net}$. The footprint

climatology represents the footprint averaged for the whole study period, which means that $\tilde{R}_{net}$ has been weighted with only one weight estimate. However, the OLS regression evaluates the energy balance closure for every half hour observation of available and turbulent energy. The evaluation of the energy balance closure by the OLS regression based on the on $\tilde{R}_{net}$ weighted by the footprint climatology is therefore a shortcoming. It would have been more correct to calculate every half hour footprint during the study period and use this to find a precise weight for the different surface types for every half hour measurement.

Another disadvantage of using the OLS regression for evaluating the energy balance closure, is the requirement of no random errors of the independent variables. This assumption is not valid when using the available energy of soil heat flux and net surface radiation as predictor variables. Therefore, the regression produces a downward bias in the regression slope coefficient, and a flatter curve is obtained. This means that the energy balance closure is found to be lower than it actually is. To avoid the incorrectly fulfillment of this assumption, Wilson et al. (2002) investigated, among other things, the performance of the reduce major axis (RMA) regression for the energy balance closure. This is simply a regression technique which switches the independent available energy and the dependent turbulent energy. The slope is then evaluated as geometric mean of the OLS and switched regression (Wilson et al., 2002). Their findings showed that when using RMA regression instead of OLS regression, the mean closure for the tested sites increased from 79% ± 1% to 83% ± 1%.

When the energy balance closure was investigated by the energy balance ratio, it was found to be 53.80% when evaluated with R_{net} from the Finse flux tower and 58.20% when evaluated with LM predicted $\tilde{R}_{net}$. Thus, the energy balance closure increased with 4.40 percent points when accounting for the heterogeneity of the surface cover. The increase is explained by the fact that the accumulated LM predicted $\tilde{R}_{net}$ during the period 18.08.18 – 25.08.18 was found to be lower than the accumulated R_{net} provided by the Finse flux tower for the same period. The effect of higher emissions of longwave radiation during night for the heterogenous surface cover, was especially important for this result.

By using EBR, it is possible to evaluate the energy balance closure overall for longer periods by averaging over random errors in the half-hour measurements. This probably explains to some extent why the energy balance closure, when evaluated with the LM predicted $\tilde{R}_{net}$, was found to be 21 percent points higher for the EBR than the OLS regression. When investigating the energy balance closure at a time scale corresponding to the half hourly measurements, there was a low balance between incoming and outgoing energy. But when the

energy balance was investigated overall for the whole period, a bigger portion of the incoming energy was explained by outgoing energy processes. For the period investigated at Finse, it was found to be a surplus of energy during daytime, while at night the negative net surface radiation and positive latent heat contributed to a deficit of energy. Therefore, a technique which investigates the energy balance by calculating the ratio between accumulated available and turbulent energy for a longer period are allowing for the surplus/deficit during day/night. For the OLS regression the same energy surplus/deficit during day/night was a major source for the flat slope, and thus the low energy closure.

In addition to measure the net surface radiation for the different surface types, a few days (19.08.18 – 21.08.18) of measurements of soil heat flux were also performed for some of the different surface types. This was done to legitimately exclude that the mismatching between the one-point measurement of soil heat flux and the footprint of the turbulent fluxes was an important cause for non-closure. The mean difference between the soil heat flux measured by the Finse flux tower and the soil heat flux measured at the different surface types were calculated to 10 Wm^{-2}. This indicated thus, as assumed, that potential differences of the soil heat flux between different surface types is not a considerable cause for the energy imbalance.

The energy storage is still unexplored at the Finse flux tower. In this study, no investigations of potential sources and sinks of energy have been performed. It remains to be investigated if storage of energy plays an important role for the energy imbalance. It is not expected that neither the physical storage of heat in the canopy nor the biochemical storage of energy in the vegetation constitute a significant contribution of the total energy storage in the surface element at Finse. This is simply explained by the scanty vegetation at place. However, the subsurface storage of energy should be explored to improve and provide more accurate estimates of the soil heat flux.

When future investigations of the energy balance for the Finse flux tower are done at longer time scales, such as a seasonal scale, storage of energy in the water should be paid attention. As shown by the surface type map (Figure 4.7), an important source of the footprint of the turbulent fluxes northwest for the tower is open water as ponds and smaller streams. According to the very high heat capacity of water, it is reasonable to assume that an extensive amount of energy is accumulated into the water masses throughout the summer season. When ignoring this effect at seasonal scale, the water ponds act like an enormous sink of energy. This leads to an incorrect evaluation of the energy balance. It could therefore be interesting to perform estimations of the energy accumulated in these sinks for future assessment of the

energy balance during summer seasons, and test whether this effect has significant influence on the energy balance ratio or not.

The advection of water in the river Utsekveikja, running southeast of the tower, was neglected in this study. Especially when the predominating wind directions are from south and east, a considerable part of the footprint of the turbulent fluxes comes from the river. Just before the river enters the source area of the flux tower, the river from lake Finsevatnet meets the meltwater and the streams from the Hardangerjøkulen Glacier. A massive amount of cold water is thus advected through and into the surface cover which is contributing to the measurements of the energy exchange. Lack of energy closure may thus be explained by missing estimates of the advected energy in the river. A project at the Department of Geosciences at the University of Oslo is investigating this potential effect. This is done by measuring the temperature and discharge at different places in the river. By comparing the measurements of these components before and after the water enters and leaves the source area of the flux tower, it is possible to estimate if any energy is accumulated and stored within the river before it is advected out of the system.

Failure to meet the requirement of a flat and homogenous surface, which is a fundamental assumption for satisfying one-dimensional transport of a single eddy covariance system used for measuring net exchange between surface and the atmosphere (Leuning et al., 2012), will be an everlasting challenge for the Finse flux tower. The fact that the Finse flux tower is placed in a highly heterogenous environment, violates the assumption that no advective flux is contributing to the exchange process. It is therefore reasonable to assume that a source of both mass and energy is advected through the measurement site. As stated by Leuning et al. (2012): "Inability to satisfy the highly demanding criterion of horizontal homogeneity in both surface fluxes and air flow is likely to be a major cause of incorrect measurements at many flux stations".

In a study that investigated the EC measurements conducted in fields with non-ideal conditions, Panin et al. (1998) pointed to the relationship between energy imbalance and the inhomogeneity of the land surface. They found a positive correlation between the increase of the heterogeneity of the surface in the vicinity of the flux tower and the increase of the energy imbalance. Because of surface inhomogeneity, a tendency of horizontal advection may generate an internal boundary layer, which cause problems for the EC measurements in the low frequency part of the covariance spectrum. As noted by Panin et al. (1998), "The point observation (instrument) interprets these influences as long waves that have an effect similar to

a process of non-stationarity". Then the lack of stationarity in the atmospheric boundary layer is important for the energy non-closure at site by contributing to the underestimation of the turbulent fluxes. A neglected transport through the sides of a terrestrial surface element is therefore invalid when the assumptions of horizontal homogeneity and steady state are not fulfilled at site, such as Finse.

Not only small-scale heterogeneity in topography and surface cover around the Finse flux tower complicates the estimation of the turbulent fluxes. The fact that the flux tower is located nearby both the lake Finsevatnet and the river Utsekveikja, may be problematic by causing breeze effects. When having two substantially different surfaces, differences in the thermal properties will occur due to different radiation properties and heat capacities of the two surfaces. The river and lake will cool and warm at a different rate than that for land. Thus, a breeze may appear. Aubinet (2008) explains that the movement of the breeze could develop in a shallow boundary layer and decouple the eddy covariance system from the surface. Such, a considerable advection of energy is likely to occur, and the turbulent transport would be poorly represented under such conditions. This leads to an underestimation of the turbulent fluxes, and the lack of capturing the energy exchange as advection increases the energy imbalance.

Another potential mechanism explaining the energy non-closure at Finse is the effect of drainage winds or mountain winds. Since the flux tower is placed in a valley, cold and dense air tends to sink down during conditions where the valley slope is cooled due to emissions of long wave radiation. The steep slope of the valley is accelerating the cold air downwards to the bottom of the valley. Here the surface is covered of flows of cold air, which creates a shallow sublayer. Aubinet (2008) states that under such conditions a decoupling between the surface and the measuring point often occurs. A considerable amount of energy can be transported by advection under these conditions. The lack of measuring the energy exchange by this mechanism is probably the most important source of error for night eddy flux measurements (Aubinet, 2008). The drainage effect at the Finse flux tower can even be strengthened by the fact that Hardangerjøkulen Glacier is located just a few kilometers southwest of the tower. Potential katabatic winds during daytime can cause erroneous estimates of the turbulent fluxes due to a decoupling between the surface and measuring point even during daytime.

As discussed, there are many potential sources explaining the low energy balance closure found at the Finse flux tower in this study. Further investigations of the potential causes will hopefully give a better understanding of the energy exchange processes and their significance for the energy balance closure.

6   Conclusion

This study has demonstrated that there is a significant difference of net surface radiation for the different alpine surface types investigated at the Finse flux tower. This implies that considerable differences occur between the surface cover which contributes as source area to the measurements of the turbulent fluxes. One should therefore strive to obtain an estimation of net surface radiation which accounts for the heterogeneity of the surface cover. An increase of 4.40 percent points was found for the energy balance closure (evaluated with the EBR) when correcting for the non-corresponding footprint between net surface radiation and the turbulent fluxes. When evaluated with OLS regression no effect on the energy balance closure was found when the non-corresponding footprint was corrected. The energy balance closure was found to be 37% when investigated with the LM predicted $\tilde{R}_{net}$ through the OLS regression, and 58% when investigated with the LM predicted $\tilde{R}_{net}$ through the EBR. The disagreement between the different techniques is most likely to be explained by EBR's advantage of evaluating the energy balance closure at longer time scales than the half-hour measurements. The EBR allows for the accumulated surplus of energy during day and the accumulated deficit of energy during night. The unfulfilled assumption of no random errors in the net surface radiation and soil heat flux, may also contribute to an underestimation of the energy balance closure when evaluated with the OLS regression.

A very high accuracy was found when predicting net surface radiation for the different surface types by using linear regression model with incoming longwave and shortwave radiation. An exceedingly large increase of the RMSE to the RMSEP of the ANNs revealed that the ANNs were overfitted. They also failed to predict the extremes and big variation of net surface radiation which occurred during daytime. Therefore, the study concludes that the ANNs are not preferable when predicting net surface radiation for small data sets (≤ 50 observations) of climatic variables.

The work presented here, is a proof-of-concept study, showing how heterogeneity at flux sites can be accounted for. At the Finse flux tower, the unfulfilled conditions of the EC-system and the large-scale heterogeneity (in terms of the glacier, the river and the valley) surpasses the effect of the net surface radiation corrected for the heterogeneity of the surface. Even though this study did not find a major increase in the surface energy balance closure, it still demonstrates the importance of accurate estimation of net surface radiation for different surface types.

References

Abbot, E., A., Gillespie, A., R., and Kahle, A., B. (2013). Thermal-infrared imaging of weathering and alteration changes on the surfaces of basalt flows, Hawai'i, USA. *International Journal of Remote Sensing* 34, (9-10), 3332-3355.

Aubinet, M. (2008). Eddy covariance CO2 flux measurements in nocturnal conditions: an analysis of the problem. *Ecological applications* 18, (6), 1368-1378.

Baldocchi, D., Falge, E., Gu, L., Olson, R., Hollinger, D., Running, S., Anthoni, P., Bernhofer, C., Davis, K., Evans, R., Fuentes, J., Goldstein, A., Katul, G., Law, B., Lee, X., Malhi, Y., Meyers, T., Munger, W., Oechel, W., Paw, K. T., Pilegaard, K., Schmid, H. P., Valentini, R., Verma, S., Vesala, T., Wilson, K. and Wofsy, S. (2001). FLUXNET: A new tool to study the temporal and spatial variability of ecosystem-scale carbon dioxide, water vapor, and energy flux densities. *Bulletin of the American Meteorological Society* 82, (11), 2415-2434.

Bonan, G. (2016). *Ecological climatology* (Third edition). Cambridge University Press, Cambridge. 692 pp.

Brewster, M. Q. (1992). *Thermal radiative transfer and properties*. John Wiley and Sons, New York. 537 pp.

Bryn, A. (n. d.) Personal communication.

Bryn, A. and Horvath, P. (2017). Nature type and vegetation around the flux tower at Finse, Hardangervidda. Unpublished vegetation map. Natural History Museum, University of Oslo.

Caner, M., Gedik, E. and Kecebas, A. (2011). Investigation on thermal performance calculation of two type solar air collectors using artificial neural network. *Expert Systems with Applications* 38, (3), 1668-1674.

Eshwar, D. and Pal Singh, D. (2012). Artificial neural network for pattern reorganization. *International Journal of Information and Computation Technology* 2, (3), 189-195.

Finkelstein, P. and Sims, P. F. (2001). Sampling error in eddy correlation flux measurements. *Journal of Geophysical Research* 106, (D4), 3503-3509.

Foken, T. (2008a). *Micrometeorology.* Springer. 306 pp.

Foken, T. (2008b). The energy balance closure problem: an overview. *Ecological Applications* 18, (6), 1351-1367.

Foken, T. and Oncley, S. (1995). Workshop on Instrumental and Methodical Problems of Land Surface Flux Measurements. *Bulletin of the American Meteorological Society* 76, (7), 1191-1193.

Foken T. and Wichura. B. (1995). Tools for quality assessment of surface-based flux measurements. *Agricultural and Forest Meteorology* 78, (1-2), 83-105.

Frost, G. V. and Epstein, H. E. (2014). Tall shrub and tree expansion in Siberian tundra ecotones since the 1960s. *Global Change Biology* 20, (4), 1264-1277.

Gershenson, C. (2003). *Artificial Neural Networks for Beginners.* Available at https://www.researchgate.net/publication/1956697_Artificial_Neural_Networks_for_Beginners (Accessed: 21.03.18)

Geraldo-Ferreira, A., Soria-Olivas, E., Serrano-López, A. and López-Baeza, E. (2011a). Estimating net radiation at surface using artificial neural networks: a new approach. *Theoretical and Applied Climatology* 106, 263-279.

Geraldo-Ferreira, A., Soria-Olivas, E., Gómez-Sanchis, J., Serrano-López, A., Velázquez-Blazquez, A. and López-Baeza, E. (2011b). Modelling net radiation at surface using "in situ" netpyrradiometer measurements with artificial neural networks. *Expert Systems with Applications* 38, 14190-14195.

Gjessing, Y. (1997). Klima og glasiologi på Finse. *Finse – et senter for høyfjellsforskning. Et skrift til 25 års jubileet for Høyfjellsøkologisk forskningsstasjon, Finse.* Høyfjellsøkologisk forskningsstasjon, Finse.

Günther, F. and Fritsch, S. (2010). neuralnet: Training of Neural Networks. *The R Journal* 2, 30-38.

Haverd, V., Cuntz, M., Leuning, R. and Keith, H. (2007). Air and biomass heat storage fluxes in a forest canopy: Calculation within a soil vegetation atmosphere transfer model. *Agricultural and Forest Meteorology* 147, 125–139.

Heusinkveld, B.G., Jacobs, A.F.G, Holtslag, A.A.M., Berkowicz, S.M. (2004). Surface energy balance closure in an arid region: role of soil heat flux. *Agricultural and Forest Meteorology* 122, 21-37.

Iziomon, M. G., Mayer, H. and Matzarakis, A. (2000). Empirical models for estimating net radiative flux: A case study for three mid-latitude sites with orographic variability. *Astrophysics and Space Science* 274, (1-4), 313-330.

Kartverket. (2018). Norgeskart.no

Kershaw, K. A. (1985). *Physiological ecology of lichens* (Re-issued 2010). Cambridge University Press. 293 pp.

Kipp & Zonen B. V. (2002). Manual version 0706. CNR1 Net radiometer Instruction Manual, Delftechpark 36, 2628 XH Delft, Holland.

Kjaersgaard, J. H., Cuenca, R.H., Plauborg, F.L. and Hansen, S. (2007). Long-term comparisons of net radiation calculation schemes. *Boundary-Layer Meteorology* 123, 417-423.

Kljun, N., Calanca, P., Rotach, M. W. and Schmid, H. P. (2015). A simple two-dimensional parameterisation for Flux Footprint Prediction (FFP). *Geoscientific Model Development* 8, 3695-3713.

Kljun, N., D'Onofrio, C., El-Madany, T., Tomelleri, E. and Wohlfahrt, G. (n.d.). *Flux Footprint Prediction (FFP) online data processing*. Available at http://geography.swansea.ac.uk/nkljun/_p/www/index.php (Accessed: 05.09.18)

Kljun, N., Rotach, M.W. and Schmid, H.P. (2002). A 3-D backward Lagrangian footprint model for a wide range of boundary layer stratifications. *Boundary-Layer Meteorology* 103, 205–226

Leinaas, H. P. and Schumacher, T. (2005). *Høyfjellsøkologi BIO1110*. Biologisk institutt, UiO. 51 pp.

Leuning, R., van Gorsel, E., Massman, W. J. and Isaac, P. R. (2012). Reflections on the surface energy imbalance problem. *Agricultural and Forest Meteorology* 156, 65-74.

LI-COR Inc (2016). EddyPro version 6.2. EddyPro Software Instruction Manual, 4647 Superior Street, Lincoln, Nebraska 68504, USA.

Mahalakshmi, D. V., Paul, A., Dutta, D., Ali, M. M., Dadhwal, V. K., Suraj Raddy, R., Jha, C. S. and Sharma, J. R. (2016a). Estimation of net surface radiation using eddy flux tower data over a tropical mangrove forest of Sundarban, West Bengal. *Geofizika* 33, (1), 1-14.

Mahalakshmi, D. V., Paul, A., Dutta, D., Ali, M. M., Suraj Reddy, R., Jha, C. S., Sharma, J. R. and Dadhwal, V. K. (2016b). Estimation of net surface radiation from eddy flux tower measurements using artificial neural network for cloudy skies. *Sustainable Environment Research* 26, 44-50.

Majozi, N. P., Mannaerts, C. M., Ramoelo, A., Mathieu, R., Nickless, A. and Verhoef, W. (2017). Analysing surface energy balance closure and partitioning over a semi-arid

savanna FLUXNET site in Skukuza, Kruger National Park, South Africa. *Hydrology and Earth System Science* 21, (7), 3401-3415.

Miller, R.G. (1981). Simultaneous statistical inference. Second edition, Springer-Verlag, New York. 299 pp.

Monteith, J. H. and Unsworth M. H. (2013). *Principles of Environmental Physics: Plants, Animals, and the Atmosphere* (Fourth Edition). Elsevier. 401 pp.

Myers-Smith, I. H., Elmendorf, S. C., Beck, P. S. A., Wilmking, M., Hallinger, M., Blok, D., Tape, K. D., Rayback, S. A., Marcias-Fauria, M., Forbes, B. C, Speed, J. D. M., Boulanger-Lapointe, N., Rixen, C., Lévesque, E., Schmidt, N. M., Baittinger, C., Trant, A. J., Hermanutz, L., Collier, L. S., Dawes, M. A., Lantz, T. C., Weijers, S., Jørgensen, R. H., Buchwal, A., Buras, A., Naito, A. T., Ravolainen, V., Schaepman-Strub, G., Wheeler, J. A., Wipf, S., Guay, K. C., Hik, D. S. and Vellend, M. (2015). Climate sensitivity of shrub growth across the tundra biome. *Nature Climate Change* 5, (9), 887-891.

Oke, T. R. (1987). *Boundary layer climates* (Second Edition). Routledge, London. 435 pp.

Panin, G. N., Tetzlaff, G. and Raabe, A. (1998). Inhomogeneity of the land surface and problems in the parameterization of surface fluxes in natural conditions. *Theoretical and Applied Climatology* 60, 163-178.

Vatne, A. (2018). *Towards Continuous Estimates of Evapotranspiration in Alpine Norway, The Establishment of an Eddy Covariance system at Finse*. Master Thesis in Geoscience. University of Oslo. 59 pp.

Shuttleworth, W.J. (2012). *Terrestrial hydrometeorology*. Wiley-Blackwell. 448 pp.

Wallace, J. M. and Hobbs, P. V. (2006). *Atmospheric Science* (Second Edition). Elsevier. 483 pp.

Wilson, K., Goldstein, A., Falge, E., Aubinet, M. and Baldocchi, D. (2002). Energy balance closure at FLUXNET sites. *Agricultural and Forest Meteorology* 113, 223-243.

Yegnanarayana, B. (1999). *Artificial Neural Networks*. Prentice-Hall of India Private Limited, New Delhi. 461 pp.